May 31, 2019

DEPARTMENT OF
TRANSPORTATION

2019 JUN -3 P 2: 58

DOCKET OPERATIONS

Christopher Lieske
U.S. Environmental Protection Agency
EPA Docket Center (EPA/DC)
EPA West Room B102
1301 Constitution Avenue NW
Washington, D.C. 20460

James Tamm
National Highway Traffic Safety Administration
U.S. Department of Transportation
West Building, Ground Floor, Room W12-140
1200 New Jersey Avenue SE
Washington, D.C. 20590

Attention: NHTSA Docket ID No. NHTSA-2017-0069
               NHTSA Docket ID No. NHTSA-2018-0067
               U.S. EPA Docket ID No. EPA-HQ-OAR-2018-0283

RE: Safer Affordable Fuel-Efficient (SAFE) Vehicles Rule for Model Years 2021-2026
        Passenger Cars and Light Trucks

Dear Mr. Lieske and Mr. Tamm:

The California Air Resources Board (CARB) submits this supplemental comment concerning
additional studies to the federal dockets on the proposed Safer Affordable Fuel-Efficient
(SAFE) Vehicles Rule for Model Years 2021-2026 Passenger Cars and Light Trucks (Proposal).
Specifically, CARB is submitting Northcott et al. (2019),[1] which contains new information on
the uptake and emission of carbon dioxide (CO_2) by coastal waters, and Gleason et al.
(2019),[2] which contains new information on the feedback between wildfires and snowpack
melt. These studies were released after the closing of the period for public comment on the

---

[1] Northcott D., Sevadjian J., Sancho-Gallegos D.A., Wahl C., Friederich J., Chavez F.P. (2019) Impacts of
urban carbon dioxide emissions on sea-air flux and ocean acidification in nearshore waters. PLoS ONE
14(3): e0214403. https://doi.org/10.1371/journal.pone.0214403.
[2] Kelly E. Gleason, Joseph R. McConnell, Monica M. Arienzo, Nathan Chellman, Wendy M. Calvin. Four-
fold increase in solar forcing on snow in western U.S. burned forests since 1999. Nature
Communications, 2019; 10 (1) DOI: 10.1038/s41467-019-09935-y.

Proposal. Because these studies contain material "of central relevance to the rulemaking,"[3] CARB is submitting this letter and both studies to all three Proposal dockets.[4]

CARB noted in its initial comments on the Proposal that the United States Environmental Protection Agency (U.S. EPA) and the National Highway Traffic and Safety Administration (NHTSA) (collectively, the Agencies) have failed to analyze properly the climate impacts of the Proposal.[5] Instead, the Agencies have claimed that the impacts of climate change will be so severe that the Proposal's increase in greenhouse gas emissions (and, by extension, the long-term effects of stalling emissions progress in the auto industry) are insignificant. The Agencies' position represents an abdication of their statutory duties and responsibilities and is contrary to law.[6] The Agencies were required to analyze and consider the expected results.[7]

The attached studies further demonstrate the need for thorough, careful analysis of the Proposal's climate impacts, as well as the compelling and extraordinary conditions California faces from climate change and increased greenhouse gas emissions. In Northcott et al. (2019), the authors collected data on CO_2 concentrations over Monterey Bay (which is home to a national marine sanctuary, significant fisheries, and globally important ecosystems) using moorings and surface robots. The data document, for the first time, that CO_2 concentrations over ocean waters ebb and flow throughout the day, often peaking in the early morning – showing that a previously common scientific assumption that CO_2 concentrations over ocean waters do not vary much over time and space does not always hold true. For Monterey Bay particularly, high morning CO_2 concentrations are likely an issue because of the nearby dense, urban Santa Clara Valley and the agricultural Salinas Valley. Given the unique topography surrounding Monterey Bay, the area's winds and other atmospheric conditions in the early morning appear to concentrate CO_2 from both Valleys over the Bay. The study concludes that this previously undocumented process could increase the amount of CO_2 that coastal waters are absorbing by about 20 percent.

The higher amount of CO_2 being absorbed by Monterey Bay and likely other coastal waters than was previously understood has important ramifications for climate impacts. The more

---

[3] 42 U.S.C. § 7607(d)(4)(B)(i); see also id. § 7607(d)(7)(A) (providing that such material forms part of the administrative record for judicial review); SAFE Vehicles Rule, 83 Fed. Reg. 42,986, 43,471 (Aug. 24, 2018) (citing 49 C.F.R. § 553.23 (committing that "[l]ate filed comments will be considered to the extent practicable")).
[4] EPA-HQ-OAR-2018-0283; NHTSA-2018-0067; NHTSA-2017-0069.
[5] E.g., CARB, Comment Letter on Proposed Safer Affordable Fuel-Efficient (SAFE) Vehicles Rule for Model Years 2021-2026 Passenger Cars and Light Trucks (Oct. 26, 2018) at 82, 85, EPA-HQ-OAR-2018-0283-5054, NHTSA-2018-0067-11873 [hereinafter "CARB Comments"]; see also State of California, et al., Comment Letter on the Draft Environmental Impact Statement for the SAFE Vehicles Rule, NHTSA-2017-0069-0625.
[6] E.g., Massachusetts v. EPA (2007) 549 U.S. 497, 523-26.
[7] See, e.g., 5 U.S.C. § 553; 42 U.S.C. § 4332; 42 U.S.C. §§ 7521(a), 7607(d); 49 U.S.C. 32902; 40 C.F.R. § 1508.27; Ctr. for Biological Diversity v. Nat'l Highway Traffic Safety Admin., 538 F.3d 1172, 1216 (9th Cir. 2008) ("The impact of greenhouse gas emissions on climate change is precisely the kind of cumulative impacts analysis that NEPA requires agencies to conduct."); see also CARB Comments, 72-85, 409-13.

CO_2 dissolved in the oceans, the more acidic the ocean becomes.[8] The harmful impacts of ocean acidification have already been extensively studied and are already being seen.[9] Northcott et al. (2019) indicates these impacts are likely to accrue faster than and not be as evenly distributed as previously anticipated. Coastal waters, particularly off urban or agricultural areas like Monterey Bay, may be harmed by ocean acidification to greater degrees.

Gleason et al. (2019) documents a unique feedback loop in western forests that exacerbates climate-driven water impacts and wildfire risk. Increased wildfires in the western U.S. in recent decades has contributed to widespread forest mortality, carbon emissions, periods of severely degraded air quality, and substantial fire suppression expenditures; climate change will continue to chronically enhance the potential for western U.S. wildfire activity. And as colleagues and I have previously reported, the deposition and accumulation of black carbon in Sierra Nevada snowpack accelerates snowmelt and has negative impacts on California's water supply.[10] Gleason et al. (2019) provides new insight into the magnitude and persistence of wildfire disturbance on snowpack and water resources via black carbon and other impurities – and the melting snowpack's feedback on wildfires. In studying the albedo of snow in several areas between 1 and 15 years after a wildfire, the authors found that, over the last 20 years, there has been more than a four-fold increase in the amount of energy absorbed by snowpack because of fires across the western U.S. As a result, more than 11 percent of western forests are already experiencing earlier snowmelt because of increased wildfires. For western states that rely on snowpack and its runoff into local streams and reservoirs, earlier snowmelt is a major concern, as the volume of snowpack and the timing of snowmelt are the dominant drivers of how much water there is and when that water is available downstream – and, thus, the presence and magnitude of summer drought. The presence and magnitude of drought itself influences the frequency and degree of wildfires.

This feedback loop – wildfires expediting snowmelt, which then amplifies the frequency and magnitude of wildfires – will only be magnified as the climate continues to change. An increasingly warmer and drier climate in the western U.S. has already been documented to

---

[8] *E.g.*, Doney SC, Fabry VJ, Feely RA, Kleypas JA (2009) Ocean acidification: The other CO2 problem. Annu Rev Mar Sci 1:169–192. https://imedea.uib-csic.es/master/cambioglobal/Modulo_III_cod101608/Tema_8-acidificaci%C3%B3n/pH/annurev.marine.010908.163834.pdf.

[9] *E.g.*, Brewer, P. G.: A short history of ocean acidification science in the 20th century: a chemist's view, Biogeosciences, 10, 7411-7422, https://doi.org/10.5194/bg-10-7411-2013, 2013; *see also* Sulpis et al., (2018) Current $CaCO_3$ dissolution at the seafloor caused by anthropogenic CO_2. Proceedings of the National Academy of Sciences Nov 2018, 115 (46) 11700-11705; DOI: 10.1073/pnas.1804250115. https://www.pnas.org/content/pnas/115/46/11700.full.pdf (showing that so much CO_2 is being absorbed into the oceans that useful calcium carbonate is dissolving too fast to keep up, and parts of the seafloor are disintegrating because of it, with a layer of seafloor that does not contain calcium carbonate having risen more than 980 feet in some areas).

[10] Hadley, O. L., Corrigan, C. E., Kirchstetter, T. W., Cliff, S. S., and Ramanathan, V.: Measured black carbon deposition on the Sierra Nevada snow pack and implication for snow pack retreat, Atmos. Chem. Phys., 10, 7505-7513, https://doi.org/10.5194/acp-10-7505-2010, 2010.
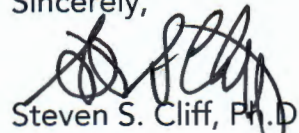
yield increased frequency, duration, and severity of both wildfires and droughts. In California, the forest mortality rate has been rising over the past two decades, posing an increasingly higher risk of wildfire in the Sierra Nevada. Climate change is already melting snowpack and increasing wildfires on its own; now, as shown in Gleason et al. (2019), the wildfire-snowpack feedback loop further amplifies the climate impacts.

As the Agencies acknowledge, the Proposal will result in a notable increase in CO_2 emissions, and yet, in the face of ample evidence of an already changing climate from unprecedented greenhouse gas emissions, the Agencies are pursing the Proposal and did not analyze how the Proposal will affect the already changing climate. The attached studies, Northcott et al. (2019) and Gleason et al. (2019), further illustrate the climate impacts already underway and that finalizing the Proposal would be arbitrary and capricious.

If you have any questions about this letter or its attached studies, please contact Attorney Wesley Dyer at (916) 445-4299 or Wesley.Dyer@arb.ca.gov.

Sincerely,

Steven S. Cliff, Ph.D
Deputy Executive Officer
California Air Resources Board

Attachments:
1. Northcott et al. (2019)
2. Gleason et al. (2019)

Four-fold increase in solar forcing on snow in western U.S. burned forests since 1999

Kelly E. Gleason[1,2], Joseph R. McConnell[1], Monica M. Arienzo[1], Nathan Chellman[1] & Wendy M. Calvin [3]

Forest fires are increasing across the American West due to climate warming and fire suppression. Accelerated snow melt occurs in burned forests due to increased light transmission through the canopy and decreased snow albedo from deposition of light-absorbing impurities. Using satellite observations, we document up to an annual 9% growth in western forests burned since 1984, and 5 day earlier snow disappearance persisting for >10 years following fire. Here, we show that black carbon and burned woody debris darkens the snowpack and lowers snow albedo for 15 winters following fire, using measurements of snow collected from seven forested sites that burned between 2002 and 2016. We estimate a 372 to 443% increase in solar energy absorbed by snowpacks occurred beneath charred forests over the past two decades, with enhanced post-fire radiative forcing in 2018 causing earlier melt and snow disappearance in > 11% of forests in the western seasonal snow zone.

[1] Division of Hydrologic Sciences, Desert Research Institute, 2215 Raggio Parkway, Reno, NV 89512, USA. [2] Department of Environmental Science and Management, Portland State University, Portland, OR 97207-0751, USA. [3] Geological Sciences and Engineering, University of Nevada, Reno, 1664 N. Virginia Street, Reno, NV 89557, USA. Correspondence and requests for materials should be addressed to K.E.G. (email: k.gleason@pdx.edu)

Most annual precipitation falls as snow in the American West[1], with mountain snowpacks serving as water reservoirs that recharge aquifers and sustain streamflow into drier summer months[2–4]. Snow is a particularly important water resource in the Intermountain West where 50–70% of precipitation is seasonally stored as snowpack. Rising air temperatures have reduced recent snowpack volume and associated seasonal snow-water storage, resulting in accelerated snowmelt and earlier springtime meltwater release[5–8], which ultimately threatens the timing and volume of downstream water resource availability[8,9]. Earlier snowmelt extends the growing season resulting in amplified late summer drought[10], reduces forest productivity limiting carbon sequestration[11], and shifts phenological synchronicity with impacts to the reproductive success of many plants, pollinators, birds, and fish[12,13]. Another consequence of climate warming and earlier snowmelt has been an increase in forest fire intensity, duration, extent, and frequency[14–16], with total area burned likely to continue increasing across the West[17–20]. The headwater regions of the Rocky Mountains are especially vulnerable, with an anticipated 300–700% increase in burned area for every 1 °C increase in global average temperature[21].

The vast majority of western forest fires occur in the seasonal snow zone, and such fires result in spatial and temporal changes in snow accumulation, ablation, and melt[22–26]. Removal of the canopy by fire results in reduced interception and enhanced snow accumulation[23,25], but the more open canopy also results in more incident sunlight on the snowpack surface[22,24], as well as changes in longwave radiation and turbulent energy fluxes[22]. In addition, increased deposition of light absorbing impurities (LAI) from the charred canopy results in reduced snow albedo[24,25]. As a result of these changes collectively referred to here as post-fire radiative forcing on snow, forest fires lead to mid-winter loss of snowpack volume[27], accelerated snowmelt, and earlier snowpack disappearance[25,28,29].

The magnitude and persistence of LAI-related albedo changes, as well as their associated radiative impacts on snow-water resources over broad scales, are presented in the current study. The extent of burned forests in the seasonal snow zone has dramatically increased across the West. While in these burned forests, 5 day earlier snow disappearance persists for >10 years following fire. Fire-related impurities, specifically black carbon and burned woody debris, darkens snowpack and lowers snow albedo for 15 winters following fire. A four-fold increase in the solar forcing on snow in western burned forests occurred from 1999 to 2018. Future increases in forest fires under a warming climate and associated radiative forcing potentially will have vast implications for the volume and timing of western streamflow and therefore water resource management[30,31].

Results

Snow disappears earlier after forest fire across the West. Satellite-based observations from 1984 to 2017 document a marked change in the forested area burned in the seasonal snow zone, increasing at an average rate of up to 9% per year ($p < 0.0001$) with a total of 1.6% of the forested area burned in 2017 alone (Fig. 1). Not all 1980s and 1990s fires were mapped in Monitoring Trends in Burn Severity (MTBS)[16], potentially resulting in a small overestimation in the trend. To assess the large-scale impacts of post-fire radiative forcing on snow, we used 2000–2016 moderate resolution imaging spectroradiometer (MODIS) satellite measurements of snow covered area across the American West to determine relative changes in snow disappearance date (SDD) before and after fire. This analysis (Methods) showed that for all studied fires in the seasonal snow

zone throughout the West ($n = 841$), snow disappeared on average 5 days earlier as a result of post-fire radiative forcing (Fig. 2). The change in relative SDD was both immediate and persistent, with the relative disappearance date remaining constant for the first seven to eight years following fire but still significantly different from pre-fire conditions even after 10 years when our analysis ended.

The change in SDD (Fig. 2) suggests that forest fires impact the snow-dominated hydrology consistently throughout the American West for at least 10 years following fire. To assess the underlying causes of this persistence, we characterized the composition, magnitude, and duration of LAI in snow samples collected in early spring 2017 from a chronosequence of seven high-severity, pine-dominated burned forests (burned from 1 to 15 years prior to sampling) located in Wyoming, Utah, and Colorado, within the headwaters for the major rivers of the American West (i.e., Columbia, Missouri, Colorado, and Rio Grande; Fig. 1; Supplementary Table 1). We first used geochemical techniques[32,33] to measure black carbon (BC; 0.09–0.6 μm) and dust (0.8–10 μm) concentrations, as well as conventional gravimetric techniques[34] to measure organic and inorganic debris (>0.7 μm) concentrations in the snow samples. We then simulated the impact of measured LAI concentrations on snow albedo using the Snow, Ice, and Aerosol Radiation (SNICAR) model[35]. We also measured the spectral albedo directly on the snow samples. Post-fire radiative forcing on snow was calculated as the modeled difference in sunlight energy absorbed by an LAI-impacted (both SNICAR-modeled and directly measured albedo) and clean snowpack (with background levels of LAI concentrations), with the former assuming full snow surface irradiance and the latter with an assumed 60% reduction from full snow surface irradiance (Methods).

Forest-fire-related impurities on snow. During the first winter following fire, BC and organic debris were highly concentrated and both declined during the 15-year chronosequence (Fig. 3; BC, $R^2 = 0.84$, p value < 0.01; organic debris, $R^2 = 0.83$, $p < 0.01$). Conversely, dust including insoluble particles and inorganic debris showed no significant changes. BC and organic debris concentrations were most variable between sites on snowpacks from more recently burned forests, and BC concentrations measured in the burned forest 15 years after fire were similar to remote pre-industrial background levels of 0.5–5 ng g^{-1} measured in ice dated from 1750 to 1850 from the Upper Fremont Glacier, Wyoming[36]. Whereas dust concentrations were variable both within and between all burned forest sites, the greatest concentrations were from the southern Rocky Mountains, a region known for dust-on-snow events[37]. Inorganic debris concentrations measured in the chronosequence samples from the southern Rockies were similar to low-dust-year concentrations measured in subalpine snowpacks in the San Juan region of the Rocky Mountains[38]. Total gravimetric LAI measured at the San Juan region sites was attributed solely to atmospheric dust deposition on snow.

Forest-fire-related solar forcing on snow. Both SNICAR-modeled and measured albedo were lowest during the first year following fire and increased during the 15-year chronosequence (Fig. 3; modeled; $R^2 = 0.81$, p value < 0.01; measured, $R^2 = 0.88$, p value < 0.01), from 0.62 to 0.68 and 0.2 to 0.51 for modeled and measured, respectively. We attribute the majority of SNICAR-modeled albedo change to BC concentrations (81% one winter following fire; 59% 15 winters following fire). Measured snow albedo incorporating impacts of both fine-grained (BC and dust) and course-grained (organic and inorganic) impurities showed
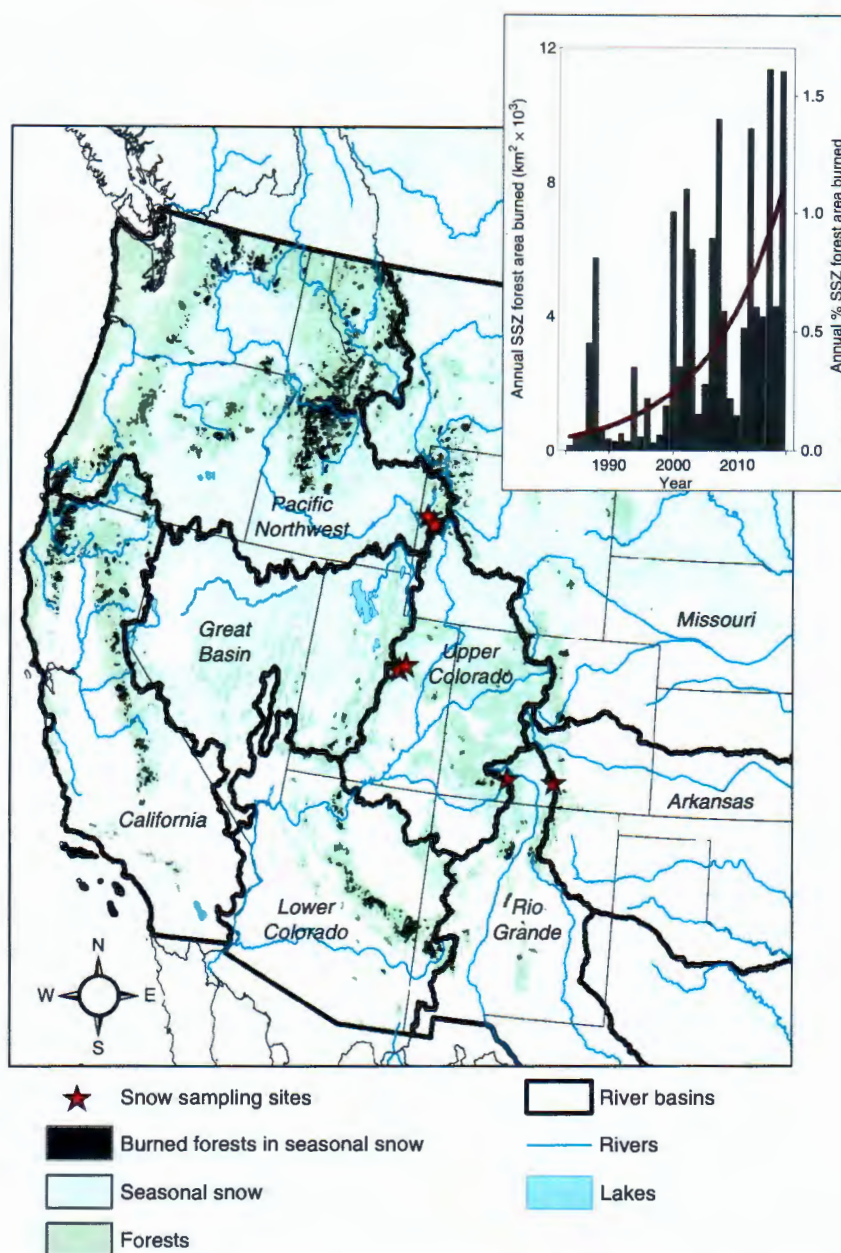
Fig. 1 Locations of forest fires in the western seasonal snow zone (SSZ) and total area burned (inset) from 1984 to 2017. Area burned determined from Landsat imagery has increased at an average rate of up to 9% per year in recent decades as a result of climate warming and a legacy of fire suppression. Also shown are 2017 snow sample collection sites located in seven recently burned forests (burned 1–15 years prior to snow sampling)

greater changes than SNICAR-modeled snow albedo that included only fine-grained (BC and dust) impurities (Fig. 3). The difference between measured and simulated snow albedo values suggests that, in addition to BC and dust, larger impurities (e.g., micro-charcoal and burned woody debris) also make critical contributions to the snowpack energy balance and ultimately snowmelt.

We determined the radiative forcing on snow associated with the SNICAR-modeled and measured albedo values using solar insolation at 40°N latitude on January 15—the day of year corresponding to maximum North American snow-covered area[39]. Calculated radiative forcing was 32 and 101 Wh m^{-2} during the first winter following forest fire for the SNICAR-modeled and measured albedo values, respectively, declining to 23 and 44 Wh m^{-2} after 15 years (Fig. 3). Combining satellite-measured

recent increases in annual burned area in forests (Fig. 1) with 15-year persistence of post-fire radiative forcing (Fig. 3) indicates a 366% recent increase in the extent of western snowpack impacted by post-fire radiative forcing (Fig. 4)—from 2.4% in 1999 to 11.2% in 2018. Using the more conservative SNICAR-modeled snow albedo values, total daily post-fire radiative forcing in the West increased 372% from 10.6×10^3 GW in 1999 to 50.0×10^3 GW in 2018. Using measured snow albedo values, total daily post-fire radiative forcing increased 443% from 23.7×10^3 GW in 1999 to 128.7×10^3 GW in 2018. For perspective, the 2018 forcing was 3.6 times the annual energy output of the Grand Coulee Dam (the largest energy producing dam in the U.S.), and sufficient energy to melt 1.4 billion m^3 (1.1 million acre-feet) of ripe (i.e., isothermal at 0 °C) snowpack. Since 1984, however, 56% of forest area burned in the western seasonal snow zone occurred in the Columbia River
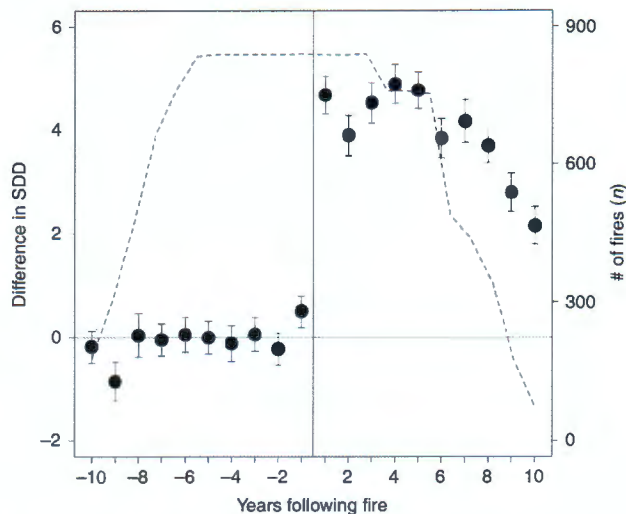
Fig. 2 Change in mean snow disappearance date (SDD) before and after fire. SDD was evaluated for all burned forests ($n = 841$; dashed line) located in the western U.S. seasonal snow zone using 2000–2016 MODIS satellite measurements. Forest fire resulted in a clear and immediate shift in SSD, with impacts of fire starting to decline after ~8 years but persisting for >10 years. Error bars indicate the standard error of the mean

Basin, the largest river by volume flowing into the Pacific Ocean from the western hemisphere, and the fourth largest river by volume in the U.S.[40]. Total daily 2018 post-fire radiative forcing on January 15 across the Columbia River Basin alone was sufficient to melt 0.82 billion m^3 (0.66 million acre-feet) of ripe snowpack, equivalent to 213% of the daily discharge on 15 January or 0.35% of annual Columbia River discharge (average discharge at Vancouver, WA from 2007 to 2017). Although substantial, these estimates of total post-fire radiative forcing on snow are conservative because they were calculated on January 15 to correspond with maximum snow-cover extent but when insolation is low. The majority of seasonal snow melts later in spring when insolation and thus the magnitude of post-fire radiative forcing are larger.

Discussion

Our results suggest that forest fires in the seasonal snow zone have immediate and profound impacts on snowmelt throughout burned forests in the American West, resulting in accelerated snow disappearance, earlier springtime meltwater release, and likely lower stream flows during drier summer months. Under climate warming, snowpack and associated water resource vulnerability will increase as forest fires become more frequent and extensive across the landscape[19,21,41,42]. As more snow falls as rain and less water is stored in warmer snowpacks, local forest fire effects related to earlier snowmelt also are likely to increase because, shallower snowpacks require less energy to melt, snow grain size is larger in warmer snowpacks which absorbs more sunlight energy, and shallower snowpacks accumulate greater impurity concentrations assuming no change in dry deposition of black carbon and burned organic debris. Human effects also contribute to snow-water resource vulnerability on a global scale, directly through aerosol emission/deposition of black carbon and dust on snowpack, and indirectly though greenhouse gas emissions, while simultaneously water resource demands are increasing for forest, agriculture, and urban use[41]. Forest fire effects to snow water resources are a concern for land managers and policy makers who have the common objective of optimizing consumption of natural resources while preserving the integrity

of the landscape. Operational water models must include forest fire disturbance effects on snowpack if they are to accurately predict flood risks, drought potential, and downstream water resource availability.

Methods

Remote sensing analyses. To determine the area burned each year across the West, we used the MTBS fire perimeter data product that spans the 1984–2015 Landsat record at 30 m spatial resolution[43]. Note that not all the 1980s and 1990s fires were mapped in MTBS[16], potentially introducing bias in the early part of the trend curve. In addition, we do not consider changes in fire activity prior to 1984 when Landsat 5 measurements began. For fires which occurred in 2016 and 2017 we used the Geospatial Multi-Agency Coordination Group fire perimeter data available online at http://rmgsc.cr.usgs.gov/outgoing/GeoMAC/historic_fire_data/. Here, we defined the western U.S. as the 11 western states of Arizona, California, Colorado, Idaho, Montana, Nevada, New Mexico, Oregon, Utah, Washington, and Wyoming. Within the perimeters of burned areas, we evaluated changes in burned forested area in the seasonal snow zone. Forested area was defined by tree density >20% in the LANDFIRE Existing Vegetation Cover (EVC) product[44]. The seasonal snow zone was determined using the MOD10A1 8-day snow-covered area product from MODIS as regions where snow was present in >25% of images centered on January 15 (2000–2017)[24].

We evaluated the difference in SDD before and after forest fire for all forests burned between 2004 to 2010 in the western seasonal snow zone included in the MTBS database. The SDD product was developed from 2000 to 2016 Moderate Resolution Imaging Spectroradiometer (MODIS) MOD10A1 daily 500 m snow-cover data[45] as the last day snow cover was observed (centered on the first five-day period without snow). To account for year-to-year changes in SDD resulting from meteorologic and geographic variability, we compared the SDD in forested areas inside each burn perimeter ($n = 841$) with that in a surrounding 2 km buffer. This difference in burned and unburned SDD (dSDD) was computed from 2000 to 2016 for all areas that burned between 2004 and 2010 to obtain at least five pre- and post-fire years. The pre-fire average dSDD was subtracted from each annual value to determine the change in dSDD before and after fire (Fig. 2). To account for inter-annual variability in forest cover, climate, and snowfall as well as satellite retrievals, we compared snowmelt in the burned forest to the surrounding unburned forest for 10 years of pre-fire conditions and found essentially no difference. This suggests that this approach to determining changes in SDD was valid, although we acknowledge potential biases in estimating snow cover from satellite imagery[45,46]. All spatial analyses were conducted in ArcInfo 10.4.1[47], and all statistical analyses were conducted in R version 3.3.3[48]. Statistical relationships were tested for a significance level of 0.01.

Field sampling. We sampled snow from a chronosequence of seven winter-accessible pine-dominated forests in the western seasonal snow zone that burned severely over 20 km^2 within the past 15 years. These sites were located in Wyoming, Utah, and Colorado—within the headwaters of the largest volume rivers in the West including the Columbia, Colorado, and Rio Grande Rivers (Supplementary Table 1). At each research site, we identified three replicate snow sampling locations in high-severity burned forested areas of >1 km^2 using Landsat-derived delta normalized burn ratio threshold value of >390[49]. At each sampling location, we collected a snow-surface sample, a snow-core sample of the entire snowpack, and measured snowpack properties, including snow water equivalent (SWE) and snow depth[24]. We collected the top 3 cm from a 0.5 m × 1 m plot on the snowpack surface using sterile scoops and Whirl-Pak® bags. Snow samples were kept frozen until analyzed in the laboratory. At each snow sampling location, we measured SWE using a federal snow sampler, and snow depth using a depth probe at nine randomly selected locations within a 50 m radius of each snow sample location to obtain a local average.

Spectral albedo measurements. Prior to chemical and other analyses, we decontaminated the snow samples by removing the outer 1 cm of snow on all sides as well as scraped the tops and bottoms using a pre-cleaned ceramic knife. In our cold laboratory (−15 °C), we measured spectral albedo for each 1 nm band throughout the range from 350 to 2500 nm using an Analytical Spectral Devices® Full-Range Field Spectrometer (ASD-FR) with a contact probe mounted in an opaque Teflon⁻ light exclusion chamber that held the probe 1 mm above the snow sample. We made the spectral albedo measurements relative to a Spectralon® white reference target for every 10 cm section of each snow sample. A spectral correction was applied to the original measurements to correct for the observed offset as a result of an imperfect white reference. We then integrated the spectral albedo measurements across the spectral range and normalized by the illumination spectrum for each snow-surface sample.

Geochemical analyses. After sample decontamination and spectral measurements, we divided the snow samples into three subsample sets and stored them in Whirl-Pak bags for subsequent geochemical analysis. To evaluate the mass of small light-absorbing impurities (LAI), including BC and crustal dust, one subsample set
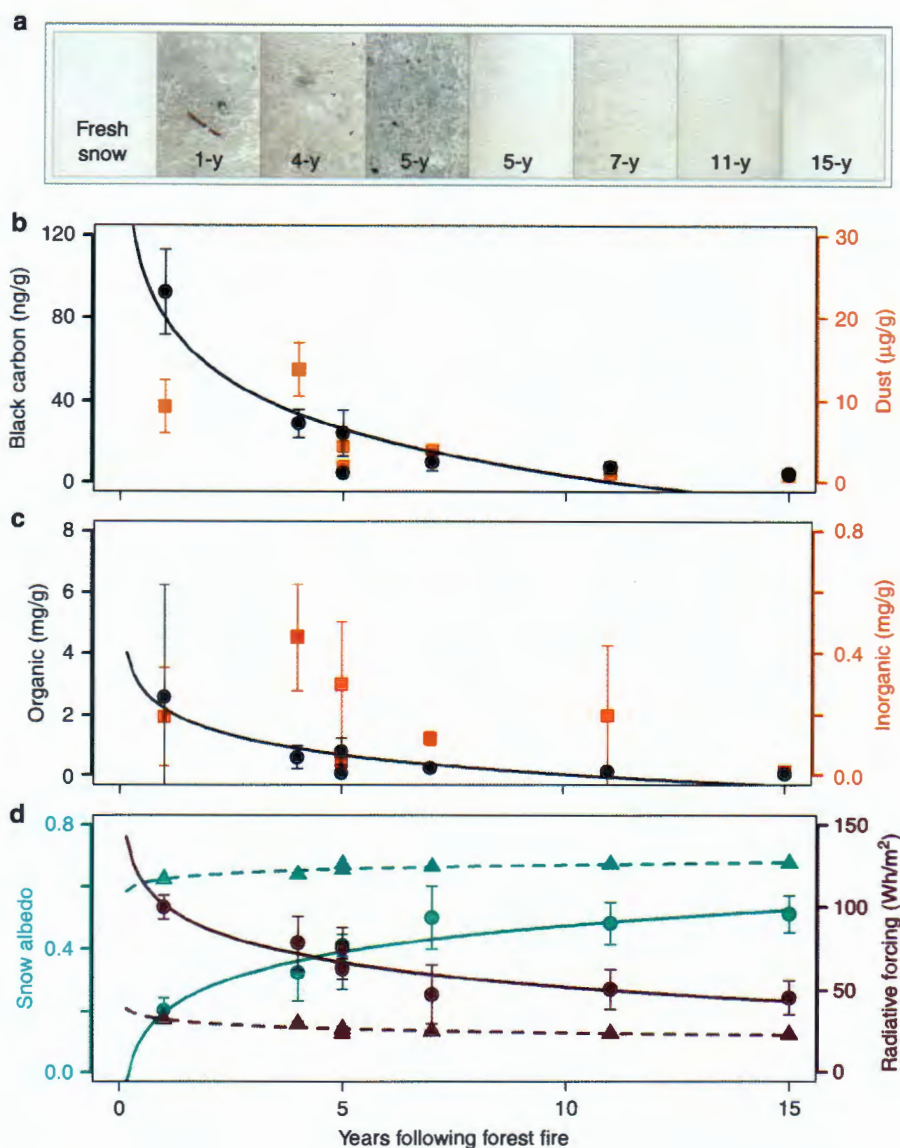
Fig. 3 Changing impacts of light absorbing impurities (LAI) on snow following fire based on 2017 sampling of chronosequence of western burned forests (Fig. 1). **a** Photographs of snow-surface samples. **b** Black carbon and dust concentrations. **c** Organic and inorganic debris concentrations. **d** Measured (dark cyan dots and solid line) and SNICAR-modeled (dark cyan triangles and dashed line) snow albedo, with associated 15 January hourly, average, post-fire radiative forcing on snow for measured (dark red dots and solid line) and SNICAR-modeled (dark red triangles and dashed line) albedo values. Error bars indicate one standard deviation

was analyzed using a continuous flow analysis system normally used for ice core measurements[32,33]. Samples were melted in Whirl-Pak bags, sonicated for 3 min, and transferred into pre-cleaned sample vials. Using an autosampler, samples were pumped through a 20 μm stainless steel filter to remove large particles (to prevent clogging the lines) and then into a low-volume debubbler[50]. From the debubbler, samples were split for measurements of BC in the size range 0.09–0.6 μm and insoluble particles used as a proxy for crustal dust in the size range 0.8–10 μm. We measured BC mass concentrations using a Single Particle Soot Photometer® (SP2; Droplet Measurement Technologies). SP2 measurements are based on incandescence. Instrument calibrations were conducted twice daily using three different standard concentrations. From replicate analyses of ice cores and snow samples, typical errors in concentration measurements are <5%[50–52]. Measurements of insoluble particle mass and size distribution were made using an Abakus® laser-based particle counter that determines semiquantitative, size-resolved particle counts[53]. Concentrations from the Abakus measurements were binned into four sizes based on requirements for the radiative transfer model (0.8–1, 1–2.5, 2.5–5, and 5–10 μm).

To verify that insoluble particle concentrations from the Abakus measurements were composed largely of crustal dust, we analyzed one subsample set for total concentrations of a broad range of elements[54] using inductively coupled plasma mass spectrometry (ICP-MS; Thermo® Element 2). Samples were melted in

Whirl-Pak bags and transferred into acid-cleaned sample vials in a class-100 clean room. Samples were then acidified to 1% HNO₃ using concentrated ultrapure nitric acid and stored for 3 months[54] prior to analysis. Ultrapure nitric acid spiked with indium was used as an external standard and introduced to the sample line just prior to sample injection into the ICP-MS instrument. Rare earth element (Ce, Dy, Gd, Pr) measurements made using the high-resolution ICP-MS confirmed that insoluble particles measured by the Abakus were composed largely of crustal dust ($r = 0.68$, $p < 0.01$).

To determine the mass and organic composition by weight of larger impurities (e.g., micro-charcoal or burned woody debris) on the snowpack, one subsample set was melted in Whirl-Pak bags and vacuum-filtered using Whatman® GF/F glass fiber filters (average pore space 0.7 μm). Using loss-on-ignition to distinguish organic vs. inorganic debris concentrations on snowpack[34], the filters were combusted in a muffle furnace for 2 h at 530 °C and the organic debris calculated as the difference in mass before and after combustion.

Radiative transfer modeling. To estimate the additional solar energy absorbed by a snowpack as a result of forest fire occurrence and subsequent deposition of LAI, we used BC and dust measurements in conjunction with the SNICAR model[35,55] (available online at http://snow.engin.umich.edu/). SNICAR uses a two-stream
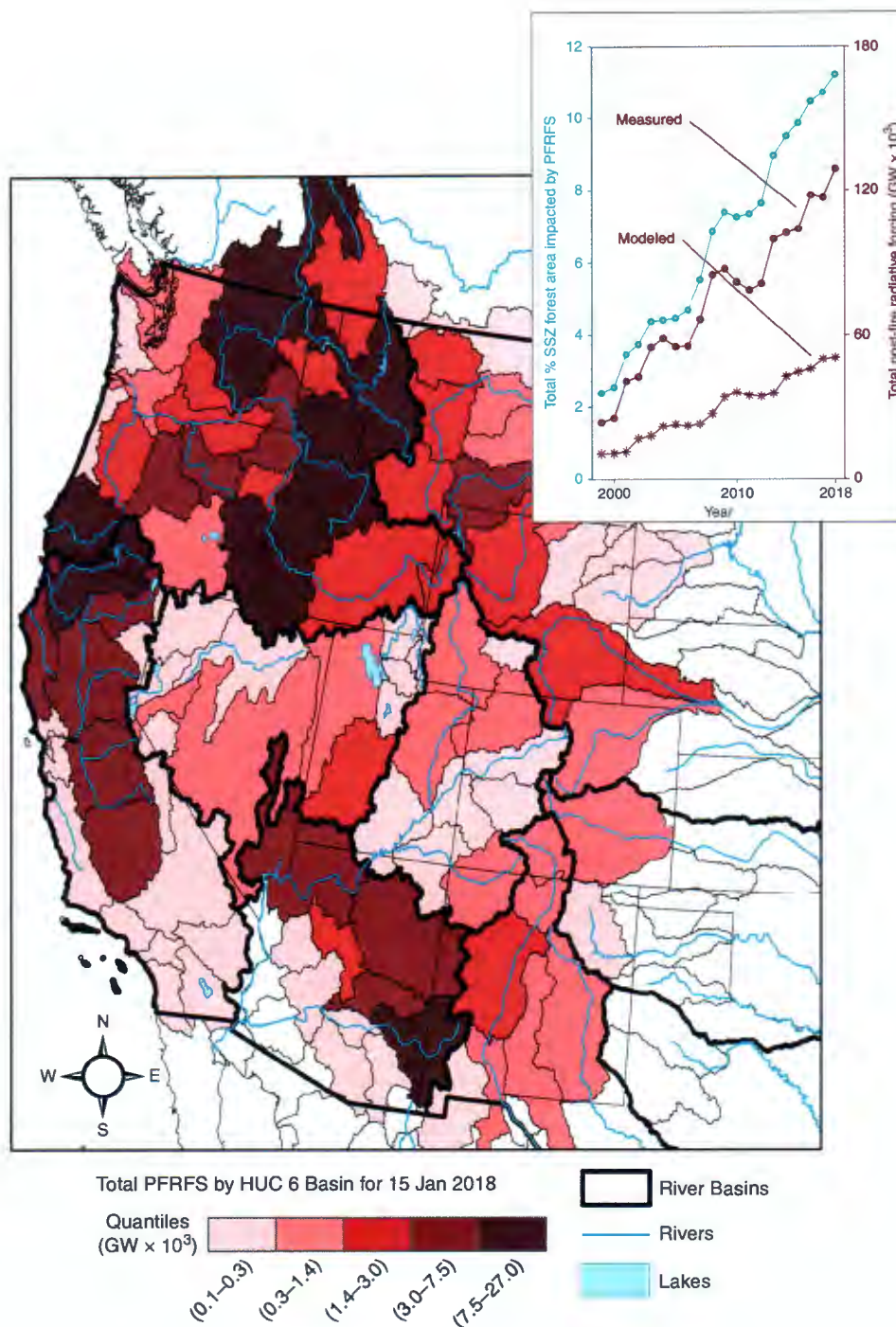
Fig. 4 Total daily post-fire radiative forcing on snow (PFRFS) in the western U.S. for 15 January 2018 based on measured albedo values from 2017 chronosequence of burned forests, and change from 1999 through 2018 based on SNICAR-modeled (red dots) and measured (red stars) albedo values (inset). A 372% (modeled) to 443% (measured) increase in post-fire radiative forcing on snow occurred since 1999, and currently over 11% of all forests in the seasonal snow zone are experiencing enhanced radiative forcing due to forest fire occurrence within the last 15 years

radiative transfer solution[56] to calculate snow albedo with known concentrations of BC and dust, snow-grain size, and incident-solar-flux characteristics. To isolate the impacts of LAI variability on radiative forcing from geographic location (e.g., slope, aspect, and latitude), we calculated the snow albedo for LAI-impacted and pristine snow using consistent parameters in SNICAR (i.e., direct radiation, effective grain size of 1500 μm, snowpack density of 300 kg m^{-2}, average solar conditions for 15 January at 40°N latitude, including 4.225 MW m^{-2} per day, solar zenith angle of 61°). The largest snow-grain size in SNICAR was selected to represent the isothermal at 0 °C snowpack consistent with field observations. We used optical parameters for hydrophobic BC in SNICAR based on the assumption that the BC was relatively recently emitted and deposited within or a short distance from the

burned forest. Because the radiative properties of larger LAI particles (e.g., micro-charcoal, burned woody debris) are not well understood and therefore not included in the SNICAR model, we also used direct spectral albedo measurements to estimate radiative forcing on snow.

Post-fire radiative forcing was calculated as the modeled difference in net snowpack shortwave radiation between the dirty (LAI-impacted) snow albedo values (both SNICAR-modeled and directly measured) and an equivalent clean snow albedo (with background levels of LAI concentrations). Background BC concentrations of 1 ng g^{-1} used in clean snow scenarios were derived from BC measurements in snow from the oldest (15-year old) fire, and were similar to pre-industrial background levels of BC in snow measured in ice dated from 1750 to

1850 from the Upper Fremont Glacier, Wyoming[36]. No background dust concentration was used in the clean snow scenarios because of the broad spatial variability in dust and that dust concentrations at each site were assumed to be unaffected by fire. A burned forest canopy with full snow surface irradiance was used for the LAI-impacted simulations. For the pristine snow simulations, we used an unburned forest canopy with a 60% reduction from full snow surface irradiance[24]. We assumed that the increase in incoming solar radiation as a result of the more open canopy was constant throughout the 15-year period of our analysis.

Geospatial analyses. To evaluate temporal variability in the maximum impact of forest fire effects to snowpack across the West for the period 1984–2017, we determined the radiative forcing each year for January 15th which is the average date of maximum North American seasonal snow cover extent[39]. Post-fire radiative forcing on snow coefficients were developed using a logistical regression of the SNICAR-modeled and measured albedo, and associated post-fire radiative forcing values during the 15 years following fire. The annual total daily post-fire radiative forcing on snow each year was calculated using the SNICAR-modeled and measured radiative forcing coefficients for the 15 years following fire (Fig. 3), applied cumulatively for the total forested area burned in seasonal snow (Fig. 1) within 15 years following fire. The spatial distribution of the post-fire radiative forcing on snow was evaluated for 2018 by integrating the radiative forcing on snow in forests burned within 15 years for each HUC 6 basin in the American West (Fig. 4).

Data availability
The authors declare that all data supporting the findings of this study are available within already existing public repositories, and the Source Data file. The MTBS data product can be found online at https://www.mtbs.gov/. The source data underlying Figs. 1a, b, 2, 3a–c, and 4a, b are provided as a Source Data file.

Code availability
The snow disappearance date and post-fire radiative forcing on snow processing scripts are available from the authors upon request. The SNICAR radiative transfer modeling scripts are available from https://github.com/EarthSciCode/SNICARv2.

References
1. Serreze, M., Clark, M., Armstrong, R., McGinnis, D. & Pulwarty, R. Characteristics of the western United States snowpack from snowpack telemetry (SNOTEL) data. *Water Resour. Res.* **35**, 2145–2160 (1999).
2. Buytaert, W., Cuesta-Camacho, F. & Tobon, C. Potential impacts of climate change on the environmental services of humid tropical alpine regions. *Glob. Ecol. Biogeogr.* **20**, 19–33 (2011).
3. Tague, C. & Grant, G. Groundwater dynamics mediate low-flow response to global warming in snow-dominated alpine regions. *Water Resour. Res.* **45**, https://doi.org/10.1029/2008WR007179 (2009).
4. Hunsaker, C. T., Whitaker, T. W. & Bales, R. C. Snowmelt runoff and water yield along elevation and temperature gradients in California's southern Sierra Nevada. *J. Am. Water Resour. Assoc.* **48**, 667–678 (2012).
5. Pederson, G., Betancourt, J. & McCabe, G. Regional patterns and proximal causes of the recent snowpack decline in the Rocky Mountains, US. *Geophys. Res. Lett.* **40**, 1811–1816 (2013).
6. Abatzoglou, J. Influence of the PNA on declining mountain snowpack in the Western United States. *Int. J. Climatol.* **31**, 1135–1142 (2011).
7. Stewart, I., Cayan, D. & Dettinger, M. Changes toward earlier streamflow timing across western North America. *J. Clim.* **18**, 1136–1155 (2005).
8. Barnett, T. P., Adam, J. C. & Lettenmaier, D. P. Potential impacts of a warming climate on water availability in snow-dominated regions. *Nature* **438**, 303 (2005).
9. Barnhart, T. B. et al. Snowmelt rate dictates streamflow. *Geophys. Res. Lett.* **43**, 8006–8016 (2016).
10. Harpold, A. A. Diverging sensitivity of soil water stress to changing snowmelt timing in the western US. *Adv. Water Resour.* **92**, 116–129 (2016).
11. Winchell, T. S., Barnard, D. M., Monson, R. K., Burns, S. P. & Molotch, N. P. Earlier snowmelt reduces atmospheric carbon uptake in midlatitude subalpine forests. *Geophys. Res. Lett.* **43**, 8160–8168 (2016).
12. Steltzer, H., Landry, C., Painter, T. H., Anderson, J. & Ayres, E. Biological consequences of earlier snowmelt from desert dust deposition in alpine landscapes. *Proc. Natl Acad. Sci.* **106**, 11629–11634 (2009).
13. Cox, C. J. et al. Drivers and environmental responses to the changing annual snow cycle of northern Alaska. *Bull. Am. Meteorol. Soc.* **98**, 2559–2577 (2017).
14. Balch, J. K. et al. Human-started wildfires expand the fire niche across the United States. *Proc. Natl Acad. Sci.* **114**, 2946–2951 (2017).
15. Westerling, A., Hidalgo, H., Cayan, D. & Swetnam, T. Warming and earlier spring increase western US forest wildfire activity. *Science* **313**, 940–943 (2006).
16. Dennison, P., Brewer, S., Arnold, J. & Moritz, M. Large wildfire trends in the western United States, 1984-2011. *Geophys. Res. Lett.* **41**, 2928–2933 (2014).
17. Williams, C. J., Pierson, F. B., Robichaud, P. R. & Boll, J. Hydrologic and erosion responses to wildfire along the rangeland–xeric forest continuum in the western US: a review and model of hydrologic vulnerability. *Int. J. Wildland Fire* **23**, 155–172 (2014).
18. Moritz, M. et al. Climate change and disruptions to global fire activity. *Ecosphere* 3, https://doi.org/10.1890/ES11-00345.1 (2012).
19. Westerling, A. et al. Climate change and growth scenarios for California wildfire. *Clim. Change* **109**, 445–463 (2011).
20. Littell, J., McKenzie, D., Peterson, D. & Westerling, A. Climate and wildfire area burned in western U. S. ecoprovinces, 1916-2003. *Ecol. Appl.* **19**, 1003–1021 (2009).
21. Council, N. R. *Climate Stabilization Targets: Emissions, Concentrations, and Impacts Over Decades to Millennia.* (National Academies Press, Washington DC, 2011).
22. Burles, K. & Boon, S. Snowmelt energy balance in a burned forest plot, Crowsnest Pass, Alberta, Canada. *Hydrol. Process.* **25**, 3012–3029 (2011).
23. Winkler, R. D. Changes in snow accumulation and ablation after a fire in south-central British Columbia. *Streamline Watershed Manag. Bull.* **14**, 1–7 (2011).
24. Gleason, K., Nolin, A. & Roth, T. Charred forests increase snowmelt: effects of burned woody debris and incoming solar radiation on snow ablation. *Geophys. Res. Lett.* **40**, 4654–4661 (2013).
25. Gleason, K. & Nolin, A. Charred forests accelerate snow albedo decay: parameterizing the post-fire radiative forcing on snow for three years following fire. *Hydrol. Process.* **30**, 3855–3870 (2016).
26. Stevens, J. T. Scale-dependent effects of post-fire canopy cover on snowpack depth in montane coniferous forests. *Ecol. Appl.* **27**, 1888–1900 (2017).
27. Harpold, A. A. et al. Changes in snow accumulation and ablation following the Las Conchas Forest Fire, New Mexico, USA. *Ecohydrology* 7, 440–452 (2014).
28. Micheletty, P., Kinoshita, A. & Hogue, T. Application of MODIS snow cover products: wildfire impacts on snow and melt in the Sierra Nevada. *Hydrol. Earth Syst. Sci.* **18**, 4601 (2014).
29. Maxwell, J. D., Call, A. & Clair, S. B. S. Wildfire and topography impacts on snow accumulation and retention in montane forests. *For. Ecol. Manag.* **432**, 256–263 (2019).
30. Hallema, D. W. et al. Burned forests impact water supplies. *Nat. Commun.* **9**, 1307 (2018).
31. Kinoshita, A. M. & Hogue, T. S. Increased dry season water yield in burned watersheds in Southern California. *Environ. Res. Lett.* **10**, 014003 (2015).
32. McConnell, J., Aristarain, A., Banta, J., Edwards, P. & Simoes, J. 20th-Century doubling in dust archived in an Antarctic Peninsula ice core parallels climate change and desertification in South America. *Proc. Natl Acad. Sci. USA* **104**, 5743–5748 (2007).
33. McConnell, J. et al. 20th-century industrial black carbon emissions altered arctic climate forcing. *Science* **317**, 1381–1384 (2007).
34. Dean Jr, W. E. Determination of carbonate and organic matter in calcareous sediments and sedimentary rocks by loss on ignition: comparison with other methods. *J. Sediment. Res.* **44**, 242–248 (1974).
35. Flanner, M., Zender, C., Randerson, J. & Rasch, P. Present-day climate forcing and response from black carbon in snow. *J. Geophys. Res.* **112**, https://doi.org/10.1029/2006JD008003 (2007).
36. Chellman, N. et al. Reassessment of the upper fremont glacier ice-core chronologies by synchronizing ice-core-water isotopes to a nearby tree-ring chronology. *Environ. Sci. Technol.* **51**, 4230–4238 (2017).
37. Painter, T. et al. Response of Colorado River runoff to dust radiative forcing in snow. *Proc. Natl Acad. Sci. USA* **107**, 17125–17130 (2010).
38. Skiles, S. & Painter, T. Daily evolution in dust and black carbon content, snow grain size, and snow albedo during snowmelt, Rocky Mountains, Colorado. *J. Glaciol.* **63**, 118–132 (2017).
39. Robinson, D. A. & Frei, A. Seasonal variability of Northern Hemisphere snow extent using visible satellite data. *Prof. Geogr.* **52**, 307–315 (2000).
40. Kammerer, J. C. Largest rivers in the United States (water fact sheet). Report No. 2331–1258 (US Geological Survey, Washington, DC, 1987).
41. Barnett, T. P. et al. Human-induced changes in the hydrology of the western United States. *Science* **319**, 1080–1083 (2008).
42. Nolin, A. & Daly, C. Mapping "at risk" snow in the Pacific Northwest. *J. Hydrometeorol.* **7**, 1164–1171 (2006).
43. Eidenshink, J. et al. A project for monitoring trends in burn severity. *Fire Ecol.* **3**, 3–21 (2007).

44. Rollins, M. G. LANDFIRE: a nationally consistent vegetation, wildland fire, and fuel assessment. *Int. J. Wildland Fire* **18**, 235–249 (2009).
45. Hall, D. K., Riggs, G. A., Salomonson, V. V., DiGirolamo, N. E. & Bayr, K. J. MODIS snow-cover products. *Remote Sens. Environ.* **83**, 181–194 (2002).
46. Parajka, J. & Blöschl, G. Spatio-temporal combination of MODIS images—potential for snow cover mapping. *Water Resour. Res.* **44**, W03406 (2008).
47. ESRI. (Environmental System Research Institute, Redlands, CA, 2015).
48. Team, R. C. (R Foundation for Statistical Computing Vienna, Austria, 2016).
49. Miller, J. & Thode, A. Quantifying burn severity in a heterogeneous landscape with a relative version of the delta Normalized Burn Ratio (dNBR). *Remote Sens. Environ.* **109**, 66–80 (2007).
50. Macdonald, K. et al. Observations of atmospheric chemical deposition to high Arctic snow. *Atmos. Chem. Phys.* **17**, 5775–5788 (2017).
51. Bisiaux, M. et al. Changes in black carbon deposition to Antarctica from two high-resolution ice core records, 1850–2000 AD. *Atmos. Chem. Phys.* **12**, 4107–4115 (2012).
52. Arienzo, M. et al. Holocene black carbon in Antarctica paralleled Southern Hemisphere climate. *J. Geophys. Res.* **122**, 6713–6728 (2017).
53. Ruth, U., Wagenbach, D., Steffensen, J. P. & Bigler, M. Continuous record of microparticle concentration and size distribution in the central Greenland NGRIP ice core during the last glacial period. *J. Geophys. Res.* **108**, 4098 (2003).
54. Uglietti, C., Gabrielli, P., Olesik, J. W., Lutton, A. & Thompson, L. G. Large variability of trace element mass fractions determined by ICP-SFMS in ice core samples from worldwide high altitude glaciers. *Appl. Geochem.* **47**, 109–121 (2014).
55. Flanner, M. et al. Springtime warming and reduced snow cover from carbonaceous particles. *Atmos. Chem. Phys.* **9**, 2481–2497 (2009).
56. Toon, O. B., McKay, C., Ackerman, T. & Santhanam, K. Rapid calculation of radiative heating rates and photodissociation rates in inhomogeneous multiple scattering atmospheres. *J. Geophys. Res.* **94**, 16287–16301 (1989).

Author contribution
The paper was written by K.E.G. and J.R.M., with input from all other co-authors; field and laboratory measurements were performed by K.E.G., M.M.A, N.C., and W.M.C., and modeling by K.E.G.; analysis and interpretation were conducted by K.E.G. and J.R.M.

Additional information
Supplementary Information accompanies this paper at https://doi.org/10.1038/s41467-019-09935-y.

Competing interests: The authors declare no competing interests.

Reprints and permission information is available online at http://npg.nature.com/reprintsandpermissions/

Journal peer review information: *Nature Communications* thanks the anonymous reviewers for their contribution to the peer review of this work.

**Publisher's note:** Springer Nature remains neutral with regard to jurisdictional claims in published maps and institutional affiliations.

Impacts of urban carbon dioxide emissions on sea-air flux and ocean acidification in nearshore waters

Devon Northcott[1]*, Jeff Sevadjian[1,2], Diego A. Sancho-Gallegos[1,3], Chris Wahl[1], Jules Friederich[1], Francisco P. Chavez[1]*

1 Monterey Bay Aquarium Research Institute, Moss Landing, CA, United States of America, 2 Scripps Institution of Oceanography, La Jolla, CA, United States of America, 3 Stanford University, Stanford, CA, United States of America

* chfr@mbari.org (FPC); dnorthcott@mbari.org (DN)
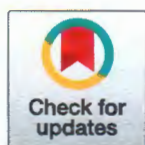
Abstract

Greatly enhanced atmospheric carbon dioxide (CO_2) levels relative to well-mixed marine air are observed during periods of offshore winds at coastal sensor platforms in Monterey Bay, California, USA. The highest concentrations originate from urban and agricultural areas, are driven by diurnal winds, and peak in the early morning. These enhanced atmospheric levels can be detected across a ~100km wide nearshore area and represent a significant addition to total oceanic CO_2 uptake. A global estimate puts the added sea-air flux of CO_2 from these greatly enhanced atmospheric CO_2 levels at 25 million tonnes, roughly 1% of the ocean's annual CO_2 uptake. The increased uptake over the 100 km coastal swath is of order 20%, indicating a potentially large impact on ocean acidification in productive coastal waters.

Introduction

The increase in atmospheric carbon dioxide (CO_2) from the burning of fossil fuels has been well documented by decades of measurements from the top of Mauna Loa on the big island of Hawaii [1]. Keeling chose the iconic Mauna Loa site because it rises into the free troposphere that is less affected by local sources of carbon pollution. Oceanographers often use well-mixed atmospheric values from similar sites or global models to estimate the sea-air exchange of CO_2 [2]. Global flux estimates find the current ocean uptake to be about two petigrams (two billion tonnes) of carbon per year [2,3]. This steady uptake of atmospheric CO_2 by the oceans results in the so-called phenomenon of ocean acidification [4]. However, studies of atmospheric CO_2 concentrations in urban environments have shown considerable enhancements of CO_2 in city centers, especially in the early morning [5,6,7], an effect known as the urban CO_2 dome. Agricultural practices can also impact local atmospheric CO_2 on a diurnal cycle with large nighttime increases due to respiration and daytime decreases associated with photosynthesis [8,9]. Near coastlines these elevated levels of CO_2 might impact marine air via atmospheric circulation and therefore increase the flux of CO_2 into nearshore waters enhancing ocean acidification. Here we present novel observations from nearshore moorings and an autonomous sea surface vehicle that show the magnitude of urban CO_2 pollution and allow us to calculate the contribution to sea-air fluxes from this previously unquantified source.

The diurnal cycles in CO_2 concentration over urban environments has been shown to peak just before sunrise at 4-5am and reach a minimum at around 4pm in the Los Angeles basin [7]. Modeling has shown similar CO_2 dome effects over the San Francisco and Monterey Bay areas [10]. However, little attention has been paid to the advection of these urban CO_2 domes over oceans and resulting impact on sea-air CO_2 flux. Monterey Bay is ideally situated for such observations, as large urban and agricultural areas in the Salinas and Silicon valleys are nearby, and a strong diurnally varying component in winds [11,12] can transport high levels of locally produced atmospheric CO_2 over the ocean. In the Monterey Bay Area the urban and agricultural CO_2 dome should reach its maximum concentrations at roughly the same time as the peak of the offshore phase of the diurnal wind cycle, leading to the advection of high CO_2 air from land sources over the coastal ocean.

As indicated above, traditional estimates of sea-air CO_2 flux are not able to quantify this nearshore phenomenon because they have a temporal or spatial scale that is too coarse to resolve these diurnally varying CO_2 anomalies. Therefore, the impact of a potentially significant source of atmospheric CO_2 on fluxes into the ocean has not previously been estimated. These impacts are magnified near urban or agricultural areas with strong offshore winds that can advect heavily polluted air over marine waters. Here we use high temporal resolution (1 hour over years) timeseries from multiple autonomous ocean based sensor platforms (moorings and surface vehicles) to provide a detailed assessment of the impacts of these high frequency variations in atmospheric CO_2 concentration on sea-air CO_2 fluxes in the nearshore environment.

Material and methods

Data sources

Data was collected from four different platforms operated by the Monterey Bay Aquarium Research Institute (MBARI) in the Monterey Bay region. Of these, three were moorings (OA1, OA2 and M1; Fig 1A) and one was an autonomous surface vehicle (Liquid Robotics Wave Glider [13]). All except M1 were outfitted with Airmar WX200 ultrasonic wind sensors which record wind speed and direction, Licor non-dispersive infrared gas analyzer CO_2 instruments which were developed to measure CO_2 concentrations in the air and water [13,14], and Seabird temperature and salinity sensors (herein CTD). M1 used an Aandara sonic anemometer together with the same CO_2 instrument and CTD. Measurements were averaged hourly in the final analysis. Wave glider measurements were taken within 5km of the Monterey Bay Time Series (MBTS) Line, a transect extending from Moss Landing out 50km along the Monterey canyon (Fig 1, red line). The moorings are located 1.5km offshore of Año Nuevo north of Santa Cruz, California (OA2), 300m off shore off of Monterey, California (OA1), and 20km offshore of Moss Landing, CA, in the center of the Monterey Bay (M1). The OA moorings are at 20 m and M1 at 1000 m depth. Wave glider data from station M, a station 220km offshore of San Luis Obispo, California (123 W 35.14 N) were also considered. Data were taken between 2013 and 2018, and all records were used, except in cases of dropout of CO_2 sensors, wind measurements, or CTD sensors. M1 recorded 1417 days of data between September 2013 and April 2018, OA1 recorded 853 days between January 2014 and July 2017, OA2 sampled 461 days between May 2015 and July 2017, and the wave glider recorded 182 days of measurements on the MBTS Line between March 2014 and March 2018.

Winds

An analysis of the phasing and length of offshore wind events was performed using the full 29 year M1 wind record. The east-west component of the winds was isolated, and binned by hour (Fig 2A). This analysis was run on both the full record, and by month to examine seasonal variations in the phasing and strength of land-sea breezes. While the strength of offshore winds
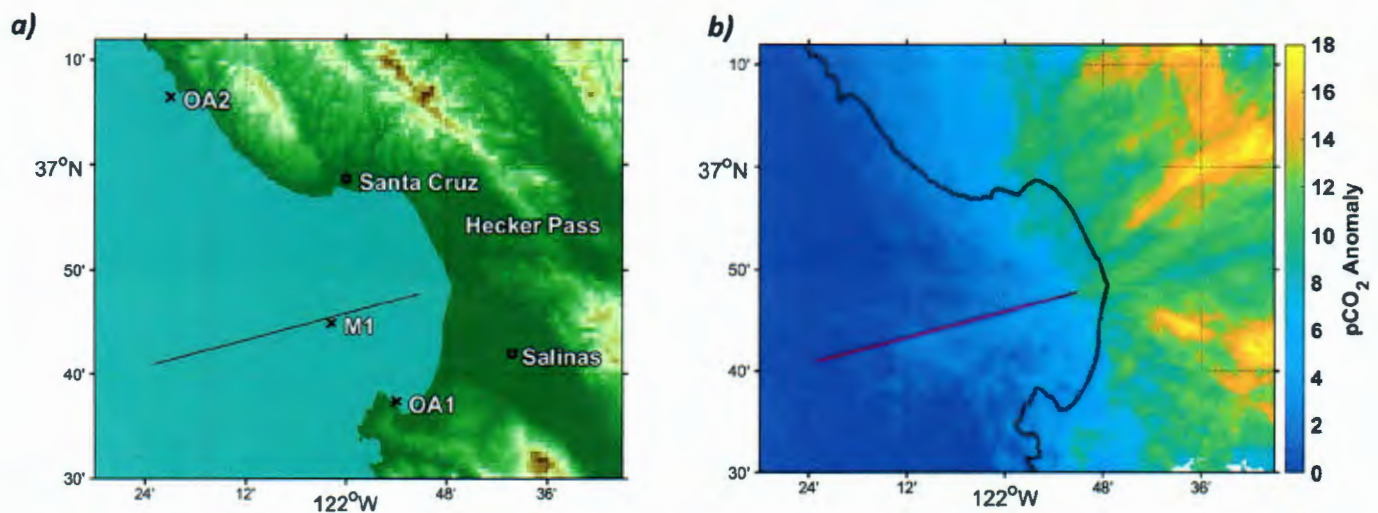
Fig 1. Location of data sources and predicted terrestrial sources of atmospheric CO₂ from wave glider data. a) Topography of the Monterey Bay area showing the location of platforms used in this study, as well as the Hecker pass and Salinas Valley, two major terrestrial sources of enhanced atmospheric CO_2 to Monterey Bay waters. The Monterey Bay timeseries (MBTS) line is also shown. b) Source regions for atmospheric CO_2 anomalies (the difference between well-mixed marine air and enhanced atmospheric CO_2; see "Anomaly Calculations" section in Methods) traced back from wave glider measurements along the MBTS Line (Fig 1A). Anomalies are particularly high in the Salinas Valley and Hecker pass areas. Anomalies are calculated for wave glider observations within 5km of the MBTS Line, and then propagated backwards for 6 hours along a path defined by wind direction and speed at the wave glider. A 5 degree uncertainty cone is drawn around the path, and all paths are averaged to yield the final figure. Coastline data republished from the Global Self-consistent, Hierarchical, High-resolution Geography Database (GSHHG) under a CC BY license, with permission from Dr. Paul Wessel, original copyright 1996.

varied by month the phasing of the cycle did not. The number of hours of offshore wind (wind direction between 0 and 165 degrees) on each fully sampled day in the record was then calculated, and these results were binned by month (Fig 2B) to give a measure of the seasonality of the persistence of offshore wind.

Atmospheric CO₂ anomaly calculations

In this paper "atmospheric CO_2 anomaly" refers to a deviation of atmospheric CO_2 values from a baseline CO_2 concentration that reflects a well-mixed atmosphere. To calculate these baseline values, a rolling median filter was applied to CO_2 measurements with duration of 15 days for moorings and 4 days for the wave glider. The filter window for the wave glider data was used because the short mission durations and high mobility of the platform lead to poor estimates of baseline pCO_2 values when the full 15 day filter window was applied. CO_2 measurements taken when the wind was blowing from the open ocean for more than 3.5 hours were used to calculate baseline values to ensure that baselines were representative of well-mixed marine air CO_2 concentrations. This baseline was then subtracted from the timeseries of atmospheric CO_2 values to yield a timeseries of atmospheric CO_2 anomalies. Comparison of the baseline pCO_2 values with NOAA's Global Greenhouse Gas (GHG) Reference Network [15] Trinidad Head station ($r^2 = 0.71$), as well as CarbonTracker [16] modeled values ($r^2 = 0.56$), showed good agreement. We used the calculated baseline pCO_2 values since these sources only run until December 2016 while our timeseries extends through early 2018.

CO₂ Fluxes

The net sea-air CO_2 flux was estimated using the equation:

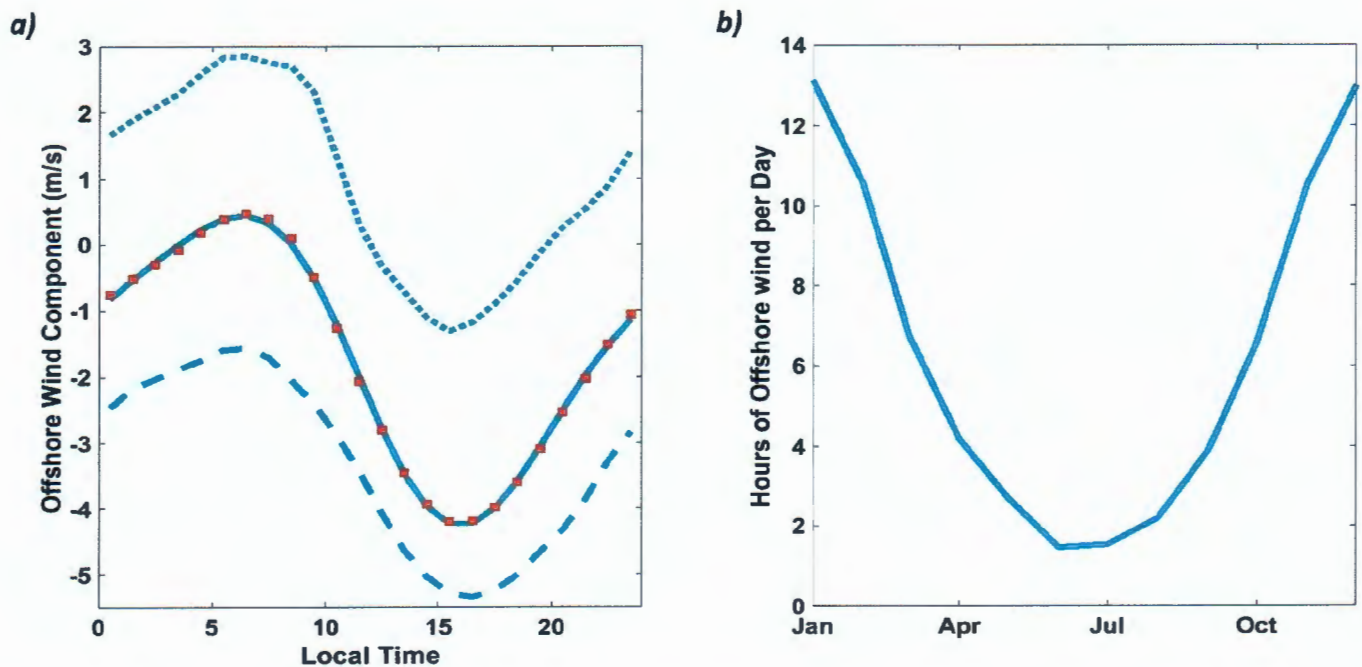$$FCO_2 = k * S * \Delta pCO_2 \tag{1}$$

Fig 2. Diurnal and annual cycles of offshore winds at the M1 mooring. a) Offshore (easterly) component of winds at the M1 mooring (see Fig 1A for location) averaged hourly. Positive (negative) values represent offshore (onshore) winds. The dotted line shows January data, representing the seasonal peak in offshore wind duration and amplitude. The dashed line represents July winds, while red squares represent full year averages, and the solid line shows the best fit to this data. Maximum offshore winds are observed at 6-7am local time. Phasing of the fit remains consistent year-round. b) Duration of offshore (0–165 degrees) winds (hours) by month over the 29 year record from the M1 mooring. There is strong correlation between daily duration of offshore wind and sea-air fluxes driven by atmospheric CO_2 anomalies (see text).

https://doi.org/10.1371/journal.pone.0214403.g002

where k is the gas transfer velocity[17], S is the solubility of CO_2 in seawater [18] and ΔpCO_2 is the difference between pCO_2 water and pCO_2 air. Gas transfer velocity is parameterized as a function of wind speed squared, while solubility is a function of water temperature and salinity. The common convention is used whereby a negative flux indicates CO_2 transfer into the ocean (a sink); while a positive flux indicates release of CO_2 into the atmosphere (a source).

Wave glider atmospheric CO_2 anomaly predictions

In order to construct a high resolution map of enhanced atmospheric CO_2 sources, anomalies were calculated for each wave glider data point. At ten minute intervals the wind speed and direction were then used to calculate the source position of the wind; this process was repeated additively over the six hours prior to any given air CO_2 measurement to construct a probable path for the measured air parcel. This method ignores local variation in wind direction and speed, mixing, and in particular excludes the effects of topography on offshore winds. In order to reduce these effects, all pixels within a five degree cone around the calculated path were assigned the value of the calculated anomaly, and added to the developing composite image containing all previous tracks. When complete the image was then divided by the number of tracks intersecting each pixel, producing an average map of probable atmospheric CO_2 anomaly sources and their strengths. This method should not be seen as providing exact locations or intensities of anomaly sources but it is straightforward and provides a general picture of the origin of strong atmospheric CO_2 anomalies.

Fluxes driven by atmospheric CO_2 anomalies

To estimate the contributions of the atmospheric CO_2 anomalies to sea-air fluxes, two flux calculations were made. The first used the well-mixed oceanic air baseline CO_2 concentrations calculated as described above. This dataset represents atmospheric CO_2 concentrations used in studies of sea-air flux that rely on modeled or well-mixed atmospheric CO_2 values. This time-series of fluxes was subtracted from a second timeseries calculated using the observed pCO_2 air concentrations. The difference between these two timeseries gives a measurement of flux due to our calculated atmospheric anomalies in air pCO_2. This method preserves the convention of negative values indicating increased transport of CO_2 into the ocean.

Results

Significant positive anomalies in atmospheric CO_2 are detected on all platforms during periods of offshore winds. A time series of atmospheric CO_2 from the OA1 mooring over 2014 and 2015 illustrates the extent of these anomalies (Fig 3). In Fig 3 a timeseries of atmospheric CO_2
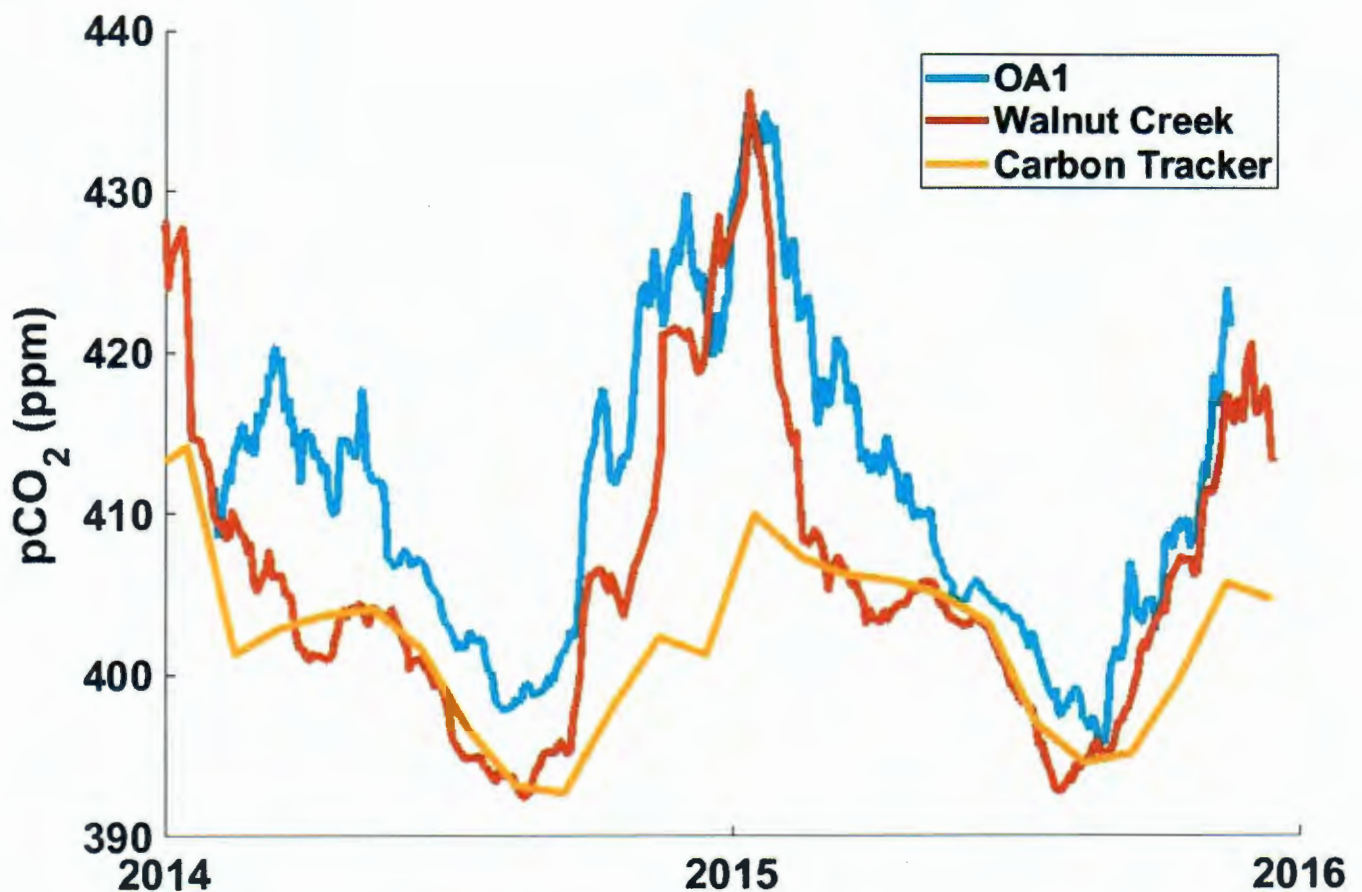

Fig 3. OA1 atmospheric pCO2 vs nearby terrestrial measurements and modeled values. OA1 mooring atmospheric CO_2 plotted with atmospheric CO_2 data measured at the NOAA GMD tower network Walnut Creek station (WGC) (Andrews, Kofler, Bakwin, Zhao, & Trans, 2009) and monthly modeled CarbonTracker CT2016 CO_2 at OA1 (Peters, et al., 2007). Tick marks represent the beginning of each year. OA1 and Walnut Creek data include periods of large atmospheric CO_2 anomalies, and were smoothed with a 15 day moving average. The CO_2 concentration at OA1 tracks that from Walnut Creek, a nearby urban location, and both differ significantly from the model that represents well-mixed marine atmospheric CO_2 concentration. Atmospheric CO_2 data collected during long periods of onshore winds (not plotted) correlates well to the CarbonTracker modeled values ($r^2 = 0.56$).
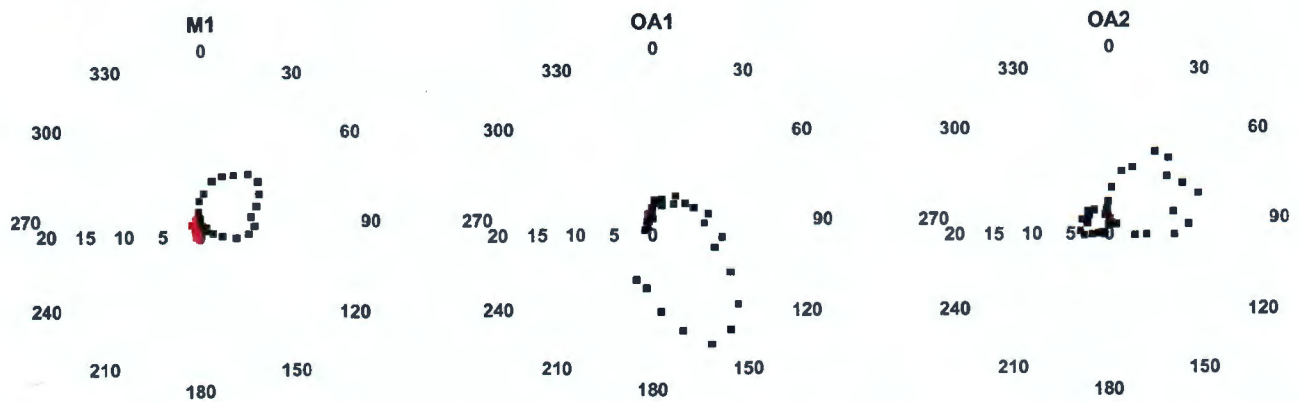
https://doi.org/10.1371/journal.pone.0214403.g003

Fig 4. CO$_2$ atmospheric anomalies (ppm) at the moorings averaged by wind direction. Anomalies are calculated as deviations from a 30-day median filtered timeseries. Positive anomalies are in black, while negative anomalies are in red. Maximum positive atmospheric CO$_2$ anomalies are found at all moorings when winds originate over land. M1 shows a double peak in anomalies related to wind direction from Hecker Pass and Salinas Valley. OA1 is very nearshore, and displays the strongest anomalies from air originating from the city of Monterey directly to its south, with a secondary peak pointing eastward toward the Salinas valley. OA2 winds are prevailing from the ocean and display weak topographic amplification, resulting in smaller anomalies that originate from urban locations in Silicon Valley.

from a nearby urban terrestrial station (Walnut Creek) [16] and clean marine air from Carbon Tracker [15] are plotted together with OA1. The similarity between OA1 and Walnut Creek is striking as are the mostly winter time increases in atmospheric CO$_2$ at both these sites relative to well-mixed marine air.

Using a basic advection model in conjunction with wave glider data (see methods) we found that the largest atmospheric CO$_2$ anomalies detected along the MBTS line originate from the Salinas valley and Hecker Pass (Fig 1B). These topographic features connect marine waters in the Monterey Bay region with large urban or agricultural areas inland and suggest that topography steers air with enhanced levels of CO$_2$ toward Monterey Bay. Hecker Pass represents a break in the mountains through which pollution from Silicon Valley can reach the coast, while the Salinas Valley contains urban centers and large agricultural fields. Binning atmospheric CO$_2$ anomalies measured at moorings by wind direction confirms sources at those locations. (Fig 4). The M1 mooring, which is situated at the center of the MBTS Line, shows a double peak in atmospheric CO$_2$ anomalies corresponding Hecker Pass (NE, 60 degrees) and the Salinas Valley (E, 100 degrees). OA1 is also impacted by CO$_2$ anomalies during periods of easterly winds from these topographic features. However, its largest anomalies are registered when winds blow from ~150 degrees. OA1 is situated only a few hundred meters north of the city of Monterey and the monthly averages at this buoy were much better correlated with the urban CO$_2$ measurements from Walnut Creek ($r^2 = 0.78$), than with Carbon-Tracker modeled atmospheric CO$_2$ ($r^2 = 0.47$) (Fig 3). This suggests that atmospheric CO$_2$ at OA1 is strongly influenced by air emanating from the city of Monterey. Meanwhile the largest atmospheric CO$_2$ anomalies at OA2 off Año Nuevo came from the northeast, directly from the Silicon Valley area (Fig 4).

Average anomalies at OA1 were close to double those at M1 during periods of offshore winds. This indicates a reduction in the strength of atmospheric CO$_2$ anomalies with distance from shore. The wave glider provides the perfect platform to further explore this relationship. Frequent wave glider measurements extend 50km out to the end of the MBTS Line, and average anomalies of 6-10ppm are detected at the end of this line during periods of offshore winds. This shows that during offshore wind events the plume of high CO$_2$ air extends at least 50km from shore, although its CO$_2$ content is reduced on average from the 15 ppm anomalies seen
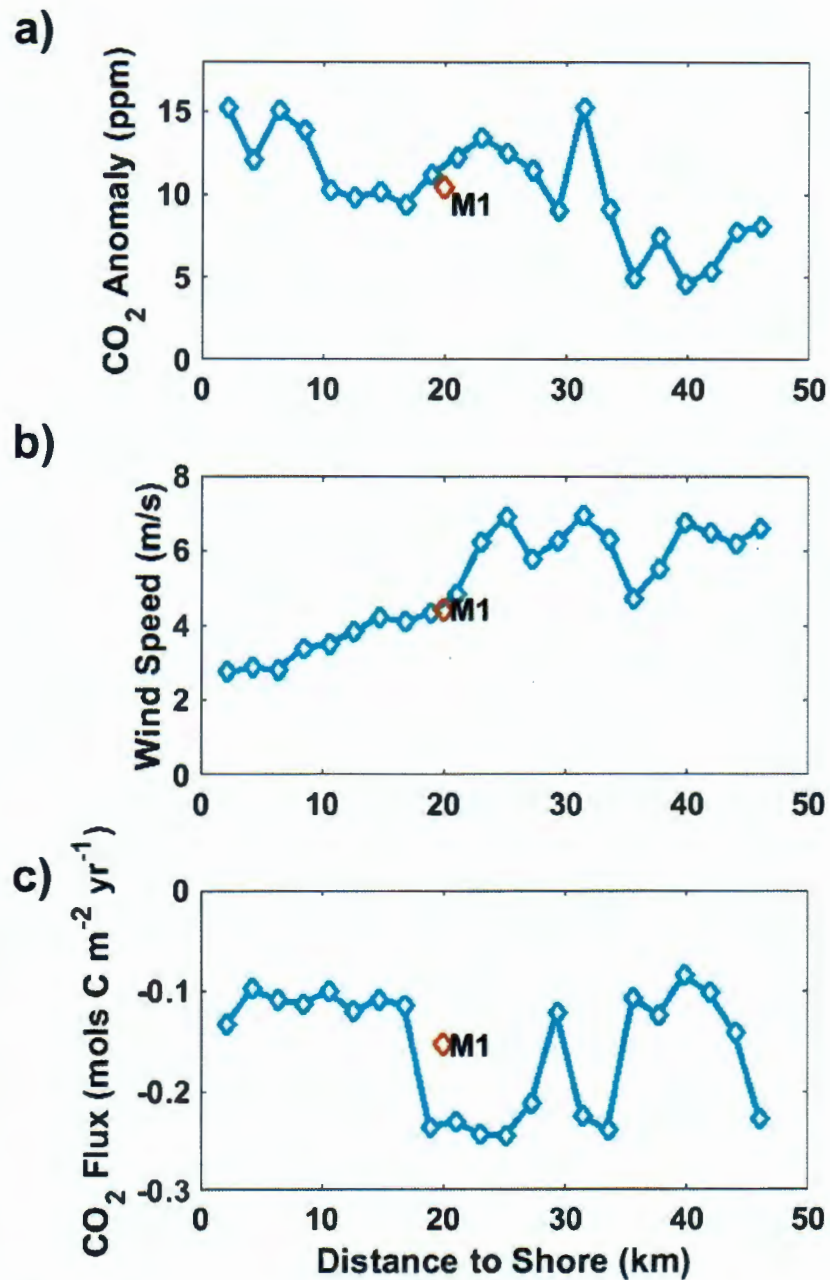
Fig 5. CO_2 anomalies, wind speed and sea-air flux anomalies along MBTS line and M1. MBTS Line wave glider and M1 measurements of (a) atmospheric CO_2 anomalies, (b) average wind speed, and (c) anomaly driven sea-air CO_2 flux, calculated during offshore wind events, and plotted against distance from shore. Anomalies are calculated by subtracting the median of persistent onshore winds. Sampling effort is biased toward the shoreward bins. A large increase in air-sea fluxes (negative flux values) is observed between 20 and 35 km offshore, driven by an increase in wind speeds with distance offshore. Meanwhile, CO_2 anomalies drop off with distance offshore. There is good agreement between the wave glider and M1 data even though these were collected over different time periods and at different resolutions.

nearshore (Fig 5). An outer limit is seen on anomaly propagation when data from station M is considered. This station is 220km offshore and routinely occupied by the wave glider. No

significant atmospheric CO_2 anomalies associated with offshore wind events are detected at this location, with all reported anomalies being within the uncertainty of the sensor. Since enhanced CO_2 levels are transported offshore by diurnal land-sea breezes, the area in which these high CO_2 levels can be observed depends on the areal extent of the land-sea breezes. The strength of offshore winds in central California varies diurnally [11,12], and the average duration of an offshore wind event at M1 is relatively short at ~6 hours. Average offshore wind speeds were 4.4 m/s, so assuming CO_2 is transported offshore at that wind speed for the duration of an offshore wind event, anomalies should rarely be detected more than 100km from the coast. This agrees with more thorough modeling and remote sensing studies that have concluded that the seaward influence of diurnal land breezes extends roughly 100km offshore along much of the west coast of the United States [19,20].

Total sea-air fluxes varied widely across the study area, largely owing to upwelling processes. OA2 sits directly in the upwelling plume off Año Nuevo where water high in carbon dioxide is brought to the surface during upwelling [13,21,22]. As a result, CO_2 flux is large and positive in recently upwelled water indicating that freshly upwelled waters are a considerable source of atmospheric CO_2. M1 is downstream from the upwelling plume, in an area where phytoplankton have increased and via photosynthesis converted much of the upwelled carbon dioxide into organic carbon. As a result average fluxes are slightly negative in this area, indicating that on an annual basis M1 is a weak sink for carbon. Inside Monterey Bay and along the southern edge fluxes are increasingly negative as the slower circulation allows phytoplankton to bloom and further reduce pCO_2. OA1 and the MBTS Line average, which is weighted to the inshore environment owing to uneven sampling effort, reflect this greater sink of atmospheric CO_2 (Fig 6).

Sea-air CO_2 fluxes due to enhanced atmospheric CO_2 were similar across all platforms. The highest atmospheric CO_2 anomaly driven fluxes were recorded at M1, reaching 0.046 mols C m^{-2} yr^{-1}. While atmospheric CO_2 anomalies were higher at OA1 owing to this mooring's close proximity to land and urban areas, a lower average offshore wind speed and a lower incidence of offshore winds reduced the effects of the higher atmospheric CO_2 on fluxes, resulting in an anomaly driven flux of 0.041 mols C m^{-2}yr^{-1}. The total annual flux along the MBTS Line was 0.030 mols C m^{-2}yr^{-1}. (Fig 6) Average fluxes were reduced over the whole line relative to M1 owing to very low wind speeds close to shore and a drop-off in anomalies beyond 35km from shore (Fig 5). OA2 recorded the lowest average anomalies, as well as the lowest percentage of offshore wind hours, but still displayed wind driven CO_2 flux anomalies of 0.019 mols C m^{-2}yr^{-1} (Fig 6). The averaged offshore profile of anomaly driven sea-air fluxes was dependent on both wind speed and atmospheric CO_2 anomalies, and was depressed inshore where wind speeds are low, and offshore where wind speed are high but atmospheric CO_2 anomalies are lower. The combination of these factors leads to a large increase in sea-air fluxes between 20 and 30 km offshore, where relatively stronger offshore winds combine with high atmospheric CO_2 anomalies (Fig 5).

Sea-air CO_2 fluxes due to atmospheric CO_2 anomalies undergo a strong seasonal cycle with increased offshore wind duration (Fig 2B) in the winter months driving larger and more frequent anomalies at all platforms. OA1 exhibits a particularly strong seasonal cycle, as strong wintertime storm winds are oriented to bring polluted air directly from the city of Monterey onto the buoy (Fig 7). At M1, where southerly storm winds come off the open ocean, a strong seasonal cycle is still present due to higher incidence of easterly and southeasterly offshores during the winter season. (Fig 2B)

Discussion

Studies of the role of the oceans in the global CO_2 budget often use low-resolution information on atmospheric CO_2 concentration to estimate sea-air CO_2 fluxes. Large scale models or
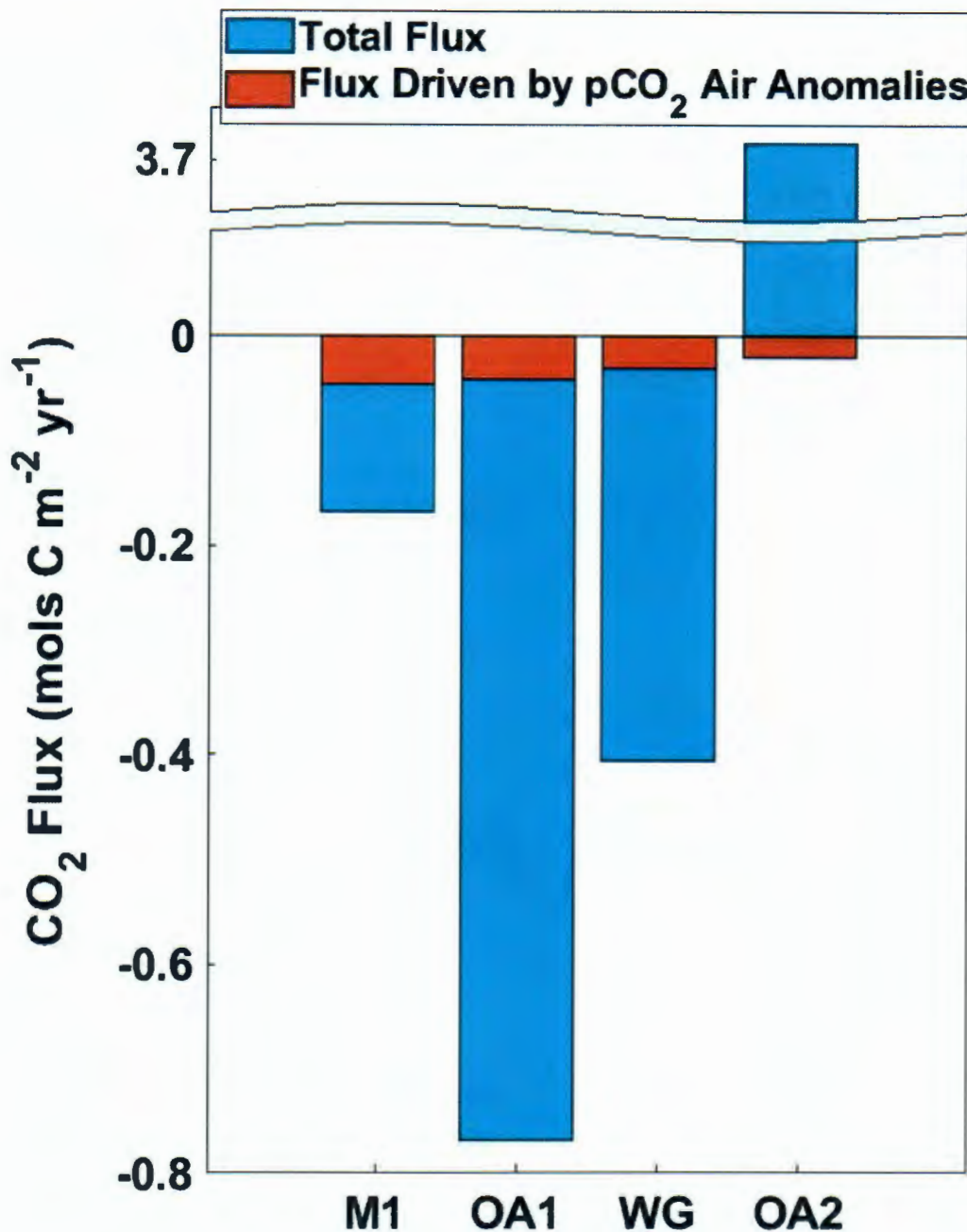
Fig 6. Yearly flux at all platforms. Sea-air CO_2 flux calculated using well mixed marine air (blue portion) together with that driven by enhanced atmospheric CO_2 (red portion) across all platforms. The striking spatial variability is evident, as is the relatively constant atmospheric CO_2 anomaly driven flux. Negative (positive) values represent uptake (loss) of CO_2 by the ocean. Increased transfer of CO_2 into the ocean due to anomalously high atmospheric CO_2 was estimated for all platforms.

https://doi.org/10.1371/journal.pone.0214403.g006

relatively few stations representative of well-mixed marine air concentrations are consistently used in flux calculations [2,23]. Observations from autonomous platforms in coastal California show that these clean air open ocean carbon dioxide concentrations are often not representative of carbon dioxide concentrations in the air nearshore. Nearshore areas experience
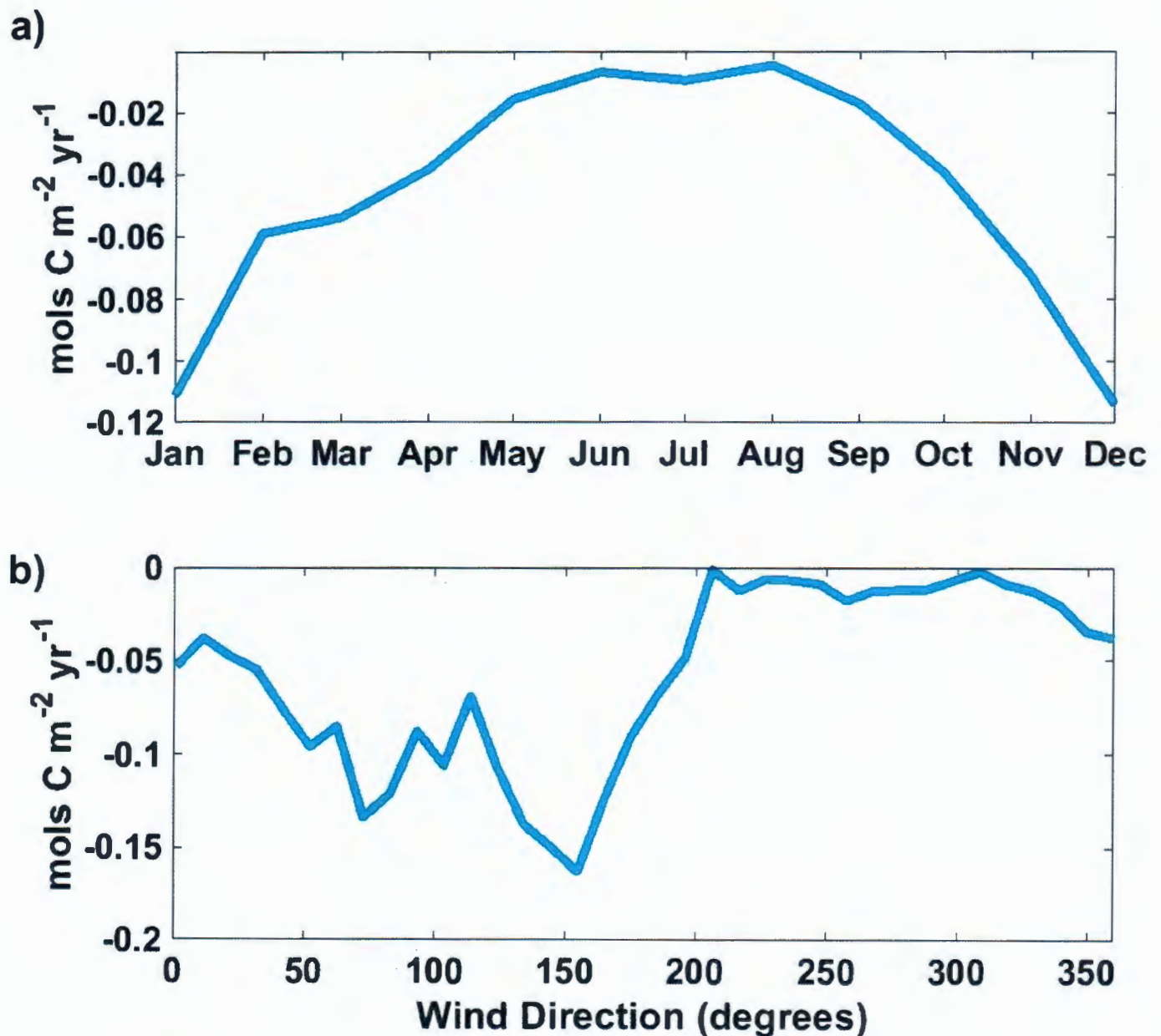
Fig 7. OA1 anomaly driven flux by month and wind direction. Atmospheric CO_2 anomaly driven sea-air flux averaged by month (a) and by wind direction (b) at OA1. Negative values indicate CO_2 flux into the ocean. Atmospheric CO_2 anomaly driven fluxes are strongest in the winter months when offshore winds are stronger and more frequent. Anomaly driven fluxes are restricted to periods of offshore winds.

significant enhancement from land sources and this impact can extend on the order of 100km from the coast. These atmospheric CO_2 anomalies, relative to well-mixed atmospheric air, contribute to sea-air fluxes regardless of the underlying oceanographic and atmospheric conditions. The association of diurnal winds to these atmospheric anomalies clearly ties them to terrestrial sources. The high frequency variability also makes it difficult to model these terrestrial sources from sparse temporal or spatial resolution datasets. High-resolution

measurements from autonomous platforms allow us to make an initial estimate of the impacts of elevated atmospheric CO2 levels from highly polluted terrestrial sources on sea-air fluxes.

The combination of offshore winds and terrestrial carbon sources drive large gradients in sea-air CO_2. However, the relatively weak offshore winds in the Monterey Bay greatly constrain CO_2 flux since it is parameterized to approach zero under very low wind speeds. This is a reasonable approximation in the open ocean where average wind speeds are rarely very low; the current parameterization may not apply when wind speeds are less than 3m/s, seriously underestimating sea-air flux at low wind speeds [17]. Average offshore wind speeds recorded along the Monterey Bay time series line never exceed 7m/s, and nearshore where CO_2 anomalies are largest wind speeds were around 3m/s. While open ocean fluxes may be accurately predicted using current sea-air flux models, our observations highlight the difficulty of using these same models in the nearshore realm, where wind speeds are lower.

The atmospheric CO_2 anomalies described above should occur anywhere that urban or agricultural areas are found near the coast, and the winds are such that they carry terrestrial sources over the marine environment. The diurnal land-sea breezes that contribute to offshore CO_2 transport observed in Monterey Bay are a widespread phenomenon worldwide [20]. While the contributions of direct CO_2 pollution to sea-air fluxes is modest, areas with stronger or more frequent offshore wind events, or larger urban centers situated closer to the water's edge should experience more significant fluxes. If the wave glider measurements in the Monterey Bay area are taken as a reasonable estimate of average anomaly driven CO_2 fluxes within 100km of land we can estimate the impact of increased atmospheric CO_2 globally. We calculated that coastal waters occupy $2.6*10^7$ km^2 or about 7% of the global ocean so the added contribution to CO_2 fluxes could be order of 25 million tonnes, or roughly 1% of the ocean's total estimated CO_2 uptake[2]. However, since this uptake is concentrated over the 100 km coastal swath the estimated sea-air flux into the ocean in these regions should be increased by around 20%. Clearly, this additional uptake of anthropogenic CO_2 will have consequences for ocean acidification [4] in nearshore regions where marine biota is concentrated. These same processes should also drive enhanced transport of other terrestrially emitted gases, aerosols, and particles over nearshore marine waters. It is therefore likely that other pollutants are also entering nearshore waters at increased rates. How these enhanced urban sources of pollution will change over time and what are their ecological impacts will need to be assessed by future studies.

Supporting information

S1 Dataset. pCO$_2$ Dataset. Dataset containing pCO$_2$ air and water measurements, as well as wind speed and direction, sea surface temperature, and salinity at all platforms.
(MAT)

Acknowledgments

Author Contributions

Conceptualization: Diego A. Sancho-Gallegos, Francisco P. Chavez.

Data curation: Devon Northcott, Jeff Sevadjian, Chris Wahl, Jules Friederich.

Formal analysis: Devon Northcott, Diego A. Sancho-Gallegos.

Funding acquisition: Francisco P. Chavez.

Investigation: Diego A. Sancho-Gallegos.

Methodology: Devon Northcott, Jeff Sevadjian, Chris Wahl, Jules Friederich.

Project administration: Francisco P. Chavez.

Resources: Chris Wahl.

Software: Devon Northcott, Jeff Sevadjian.

Supervision: Francisco P. Chavez.

Visualization: Devon Northcott.

Writing – original draft: Devon Northcott.

Writing – review & editing: Francisco P. Chavez.

References

1. Keeling CD. Rewards and Penalties of Monitoring the Earth. Annual Review of Energy and the Enviroment. 1998; 23(1): p. 25–82.

2. Takahashi T, Sutherland SC, Wanninkhof R, Sweeny C, Freely RA, Chipman DW, et al. Climatological mean and decadal change in surface ocean pCO2, and net sea-air CO2 flux over the global oceans. Deep-Sea Research II. 2009; 56: p. 554–577.

3. Bourgeois T, Orr JC, Resplandy L, Terhaar J, Ethe C, Gehlen M, et al. Coastal-ocean uptake of anthropogenic carbon. Biogeosciences. 2016; 13: p. 4167–4185.

4. Doney SC, Fabry VJ, Feely RA, Kleypas JA. Ocean Acidification: The Other CO2 Problem. Annual Review of Marine Science. 2009; 1(1): p. 169–192.

5. Idso CD, Idso SB, Balling RR. An Intensive Two Week Study of an Urban CO2 Dome in Phoenix, Arizona, USA. Atmospheric Enviroment. 2001; 35(6): p. 995–1000.

6. Kort EA, Frankenberg C, Miller CE, Oda T. Space-based observations of megacity carbon dioxide. Geophys. Res. Lett. 2012; 39(17).

7. Newman S, Jeong S, Fischer ML, Xu X, Haman CL, Lefer B, et al. Diurnal tracking of anthropogenic CO2 emissions in the Los Angeles basin megacity during spring 2010. Atmospheric Chemistry and Physics. 2013; 13(8): p. 4359–4372.

8. Verma SB, Rosenberg NJ. Carbon dioxide concentration and flux in a large agricultural region of the great plains of North America. Journal of Geophysical Research. 1976; 81(3): p. 399–405.

9. Nakadai T, Yokozawa M, Ikeda H, Koizumi H. Diurnal changes of carbon dioxide flux from bare soil in agricultural field in Japan. Applied Soil Ecology. 2002; 19(2): p. 161–171.

10. Jacobson MZ. Enhancement of Local Air Pollution by Urban CO2 Domes. Environmental Science & Technology. 2010; 44(7): p. 2497–2502.

11. Kindle JC, Hodur RM, deRada S, Paduan JD, Rosenfeld LK, Chavez FP. A COAMPS reanalysis for the Eastern Pacific: Properties of the diurnal sea breeze along the central California coast. Geophys. Res. Lett. 2002; 29(24).

12. Banta RM, Olivier LD, Levinson DH. Evolution of the Monterey Bay Sea-Breeze Layer As Observed by Pulsed Doppler Lidar. J. Atmos. Sci. 1993; 50: p. 3959–3982.

13. Chavez FP, Sevadjian J, Wahl C, Friederich J, Friederich GE. Measurements of pCO2 and pH from an autonomous surface vehicle in a coastal upwelling system. Deep Sea Research Part II: Topical Studies in Oceanography. 2017; 151: p. 137–146.

14. Friederich GE, Brewer PG, Herlien R, Chavez FP. Measurement of sea surface partial pressure of CO2 from a moored buoy. Deep Sea Research Part I: Oceanographic Research Papers. 1995; 42(7): p. 1175–1186.

15. Andrews AE, Kofler J, Bakwin PS, Zhao C, Trans P. Carbon Dioxide and Carbon Monoxide Dry Air Mole Fractions from the NOAA ESRL Tall Tower Network, 1992–2009. 2009; Version: 2011-08-31.

16. Peters W, Jacobson AR, Sweeney C, Andrews AE, Conway TJ, Masarie K, et al. An atmospheric perspective on North American carbon dioxide exchange: CarbonTracker. Proceedings of the National Academy of Sciences of the United States of America. 2007 January; 104(48): p. 18925–18930. https://doi.org/10.1073/pnas.0708986104 PMID: 18045791

17. Wanninkhof R. Relationship between wind speed and gas exchange over the ocean revisited. Limnology and Oceanography: Methods. 2014; 12: p. 351–362.

18. Weiss RF. Carbon dioxide in water and seawater: the solubility of a non-ideal gas. Marine Chemistry. 1974; 2(3): p. 203–215.

19. Perlin N, Samelson RM, Chelton DB. Scatterometer and Model Wind and Wind Stress in the Oregon–Northern California Coastal Zone. Mon. Wea. Rev. 2004 August; 132(8): p. 2110–2129.

20. Gille ST, Llewellyn Smith SG, Statom NM. Global observations of the land breeze. Geophys. Res. Lett. 2005; 32(5).

21. Chavez FP, Pennington T, Michisaki R, Blum M, Chavez G, Friederich J, et al. Climate Variability and Change: Response of a Coastal Ocean Ecosystem. Oceanography. 2017; 30(4): p. 128–145.

22. Friederich GE, Walz PM, Burczynski MG, Chavez FP. Inorganic carbon in the central California upwelling system during the 1997–1999 El Niño–La Niña event. Progress in Oceanography. 2002; 54(1–4): p. 185–203.

23. Ishii M, Feely RA, Rodgers KB, Park GH, Wanninkhof R, Sasano D, et al. Air-sea CO2 flux in the Pacific Ocean for the period 1990–2009. Biogeosciences. 2014; 11(3): p. 709–734.